Department of Physics and Astronomy
Heidelberg University

Bachelor Thesis in Physics
submitted by

Felix Fleischle

born in Mühlacker (Germany)

2024

Level-1 jet trigger performance of the Legacy and Phase-I systems at the ATLAS detector in Run-3 data

This Bachelor Thesis has been carried out by Felix Fleischle at the
Kirchhoff Institut in Heidelberg
under the supervision of
Prof. Dr. Hans-Christian Schultz-Coulon

Abstract

In order to handle the increased Luminosity in Run-3, the ATLAS Level-1 calorimeter trigger was enhanced in the scope of the Phase-I upgrade of the ATLAS detector, with the goal to replace the previous Legacy trigger system. Three new feature extractors were introduced: The Electron Feature Extractor (eFEX), the Jet Feature Extractor (jFEX) and the Global Feature Extractor (gFEX). This thesis compares the Level-1 jet trigger performance of the Legacy and Phase-I trigger systems at the ATLAS detector using Run-3 data taken during the Phase-I commissioning phase. Jet trigger efficiencies and trigger rates for all systems are presented. Single-jet and multi-jet efficiencies are calculated using a Z boson event selection. Integrated rates are calculated and compared for four different sets of triggers with matching efficiency curves. It is demonstrated that jFEX performs better compared to Legacy, with similar efficiencies and a lower rate than the Legacy system.

Kurzfassung

Um die höhere Luminosität in Run-3 zu bewältigen, wurde der ATLAS Level-1 Kalorimeter Trigger im Kontext des Phase-I Upgrades erneuert, mit dem Ziel das vorherige Legacy Trigger System abzulösen. Drei neue Feature Extractor wurden eingeführt: Der Electron Feature Extractor (eFEX), der Jet Feature Extractor (jFEX), und der Global Feature Extractor (gFEX). Diese Arbeit vergleicht die Level-1 Jet Trigger Performance des Legacy und Phase-I Trigger Systems des ATLAS Detektors in Run-3 Daten, aufgezeichnet während der Phase-I Inbetriebnahmnephase. Für alle Systeme werden Jet Trigger Effizienzen und Trigger Raten präsentiert. Single-Jet und Multi-Jet Effizienzen werden durch eine Z-Boson Selektion bestimmt. Integrierte Raten werden berechnet und für vier verschiedene Gruppen von Triggern mit übereinstimmenden Effizienzkurven verglichen. Es wird gezeigt dass jFEX eine bessere Performance aufweist als das Legacy System, mit ähnlicher Effizienz und niedrigerer Rate.

Contents

1 Introduction

Being the worlds largest particle collider, the Large Hadron Collider (LHC) has provided many great contributions to particle physics, most notably the discovery of the Higgs boson by the ATLAS and CMS experiments in 2012 [1, 2]. However, the enormous amount of particle collisions at the LHC creates many challenges in collision event processing.

As the search for new physics continues, the LHC aims to increase the centre-of-mass energy of proton-proton collisions, as well as the total amount of data gathered during run phases. Accordingly, many improvements were installed to the LHC during the shutdown period between Run-2 and Run-3 from 2019 to 2022. To match the increased performance of the LHC, the ATLAS detector has commissioned the Phase-I upgrade, introducing a large number of changes to the detector configuration compared to the previous configuration - the Legacy system. In order to handle the increased average Luminosity of the LHC in Run-3, the Level-1 trigger system of the ATLAS detector was revamped. During the commissioning phase, both the Legacy and Phase-I trigger systems are still active, paving the way for performance analyses on the new system compared to the Legacy system, which provide important feedback to the hardware community.

Many ongoing physics analysis projects rely on cones of particles from hadronisation, so-called jets, such as the decay of a Higgs pair into four jets [3]. Thus, it is crucial to ensure that events containing these jets are triggered correctly by the trigger system to prevent any loss of potential data, while making use of the trigger rate budget of the ATLAS trigger efficiently.

The analysis performed in this thesis targets the Level-1 jet trigger performance for the Phase-I system in comparison to the Legacy system. For the performance of a trigger, both the trigger efficiency and the trigger rate are crucial quantities. Accordingly, the Level-1 jet trigger performance is evaluated by taking both the Level-1 single-jet efficiencies and multi-jet efficiencies, as well as their respective trigger rates into account.

The theoretical background on the Z boson events occurring at the LHC which will be used for convenient event selection in the analysis are covered in Section 2. In Section 3, an overview of the Run-3 configuration of the ATLAS detector is provided, and the Phase-I upgrade to the Level-1 trigger system is summarised.

With the necessary background covered, the then remaining Sections will focus on the steps taken in this performance analysis: To enable an accurate efficiency calculation, an efficiency framework was built in the scope of this thesis, implementing calibration and cleaning of physics objects, as well as overlap removal, laying the groundwork for the efficiency calculations. The framework construction is covered in Section 4. In Section 5, single-jet efficiencies were determined for the Phase-I and Legacy systems. Section 6 describes the process of calculating multi-jet efficiencies and its results. To accurately compare Phase-I and Legacy performance, efficiency-matched rate comparison was performed. The necessary steps and calculations are summarised in Section 7. Finally, the results of this trigger performance analysis are summarised in Section 8.

2 The Drell-Yan Process

The Z boson is a neutral gauge boson which carries the weak force. In the LHC, the Z boson is produced in the Drell-Yan process [4], which is illustrated in Figure 1.
In the leading order process $q\bar{q} \rightarrow Z/\gamma \rightarrow l\bar{l}$, a quark from the proton-proton collision and the

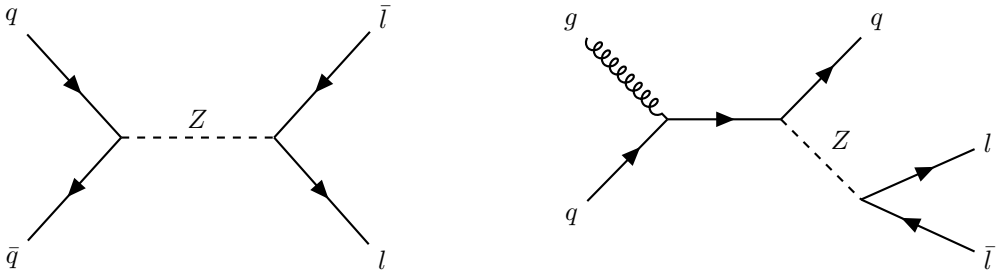

Figure 1: The Drell-Yan process in the leading order (a) and next to leading order (b).

corresponding sea anti quark annihilate to a Z boson, which then produces a lepton/anti lepton pair.
In the next to leading order process $qg \rightarrow qZ/\gamma \rightarrow ql\bar{l}$, an extra quark occurs in the final state, which can cause hadronisation and produce a jet.
The leading order process contributes roughly 65% of the cross section, with the dominant next to leading order process accounting for approximately 35% [4].
Taking these numbers into account, the Drell-Yan process and Z boson events show three important properties:

- They are easy to filter out of a larger set of events, due to the two oppositely charged leptons in the final state and the well known mass of the Z boson.
- They provide a high cross section for jets in the final state.
- There are always leptons present in the final state independent of jets.

This thesis will make use of these three properties for the efficiency calculations, which will be covered in Section 5.

3 The Large Hadron Collider and the ATLAS Detector

The Large Hadron Collider (LHC) [5] near Geneva, Switzerland is currently the worlds most powerful particle collider with a circumference of 26.7 km and a centre-of-mass energy of up to $\sqrt{s} = 13.6$ TeV [6].
The LHC is mainly a proton-proton collider, where the two proton beams circulate in separate beam pipes clockwise and counter-clockwise respectively. The beams are structured into bunches of approximately 10^{11} protons, with 3564 bunch slots per beam, of which only 2808 are filled. Every single bunch is focused to about 30 cm, or 1 ns in terms of temporal spacing, and the bunches are separated from each other in time by 25 ns. The proton beams are focused by superconducting magnets.
There are four main experiments located at the LHC: The ATLAS and the CMS experiments, which are multi-purpose detectors, as well as the LHCb experiment, which focuses on measurements of the flavour sector of the Standard Model, and the ALICE experiment specialising in heavy ion collisions.

3.1 The ATLAS Detector

With its 25m in height, 44m in length and about 7000 t, the ATLAS detector was designed for a peak instantaneous Luminosity (see Appendix A.1) of $\mathcal{L} = 10^{34}\,\mathrm{cm}^{-2}\mathrm{s}^{-1}$ at a centre-of-mass energy of $\sqrt{s} = 14\,\mathrm{TeV}$ [6]. It consists of many detector sub-systems, as well as two magnet systems, that allow for identification of the charge and momentum of all produced particles. An overview of the current Run-3 configuration of the detector can be seen in Figure 2.

The Inner Detector

The innermost detector sub-system is the Inner Detector (ID) [6]. Its main purpose is the reconstruction of trajectories of all electrically charged particles created in the collisions. It consists of three different detectors: The Silicon Pixel Detector with the highest granularity, which covers the vertex region and provides the first four measurements per track, the Semiconductor Tracker, which usually allows for eight measurements, and the Transition Radiation Tracker, which radially extends the track reconstruction.
The information gained by the ID plays an important role in particle identification, as well as measurement of transverse momentum. Additionally, it allows for the reconstruction of the primary and secondary vertices of the interactions. It covers a Pseudorapidity (see Appendix A.2) range of $|\eta| < 2.5$.

The Calorimeter System

The calorimeter system [6] provides precise energy measurements of interacting particles by containing the showers of particles from electromagnetic and strong interactions. Additionally, the shower shape can be observed from positional information, which allows for further particle identification. An overview of the ATLAS calorimeter system can be found in Figure 3.

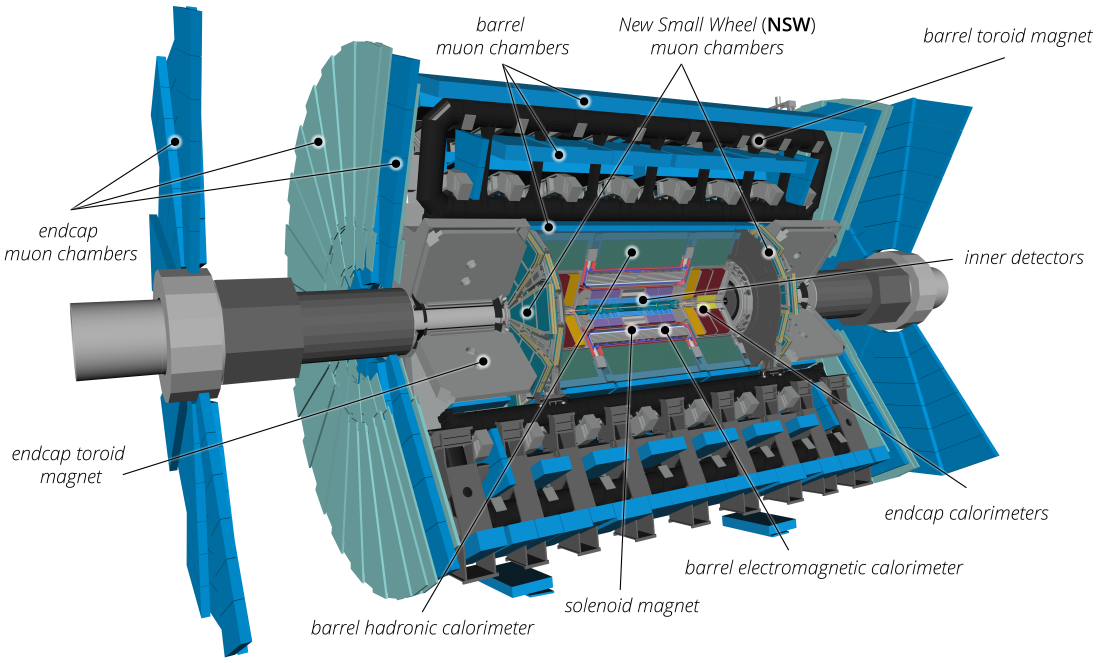

Figure 2: Cut-away view of the Run-3 configuration of the ATLAS detector indicating the locations of the larger detector sub-systems. [6].

The calorimeter system consists of two different calorimeters, both of which are sampling calorimeters. The first calorimeter is the Liquid Argon (LAr) calorimeter. It can be divided into the LAr Electromagnetic Barrel (EMB), the LAr Electromagnetic Endcap (EMEC), the LAr Hadronic Endcap (HEC), as well as the Forward Calorimeter (FCal), covering a total range of $|\eta| < 4.9$. The barrel and endcap cover a range of $|\eta| < 3.2$, while the FCal extends the calorimetry to the full η range.
The second calorimeter system is the Tile calorimeter, using scintillator tiles and steel. It covers a range of $|\eta| < 1.7$, and can be divided into the Tile Long Barrel surrounding the EMB, and Tile Extended Barrel.

The Muon Spectrometer

The outermost detector sub-system is the muon spectrometer [6]. Since muons can penetrate both calorimeters, they are the only particles that can escape the ATLAS detector together with neutrinos. Hence, the muon spectrometer is placed at the end of the detector to reconstruct the trajectories of passing muons. It consists of separate trigger and tracking chambers measuring the deviation caused by the magnetic field generated by the toroidal magnets.

Trigger and Data Acquisition System

The Trigger and Data Acquisition (TDAQ) system selects and reads out interesting events for further offline processing [6].
Due to the high collision frequency of 40 MHz and the large event data size, not every single

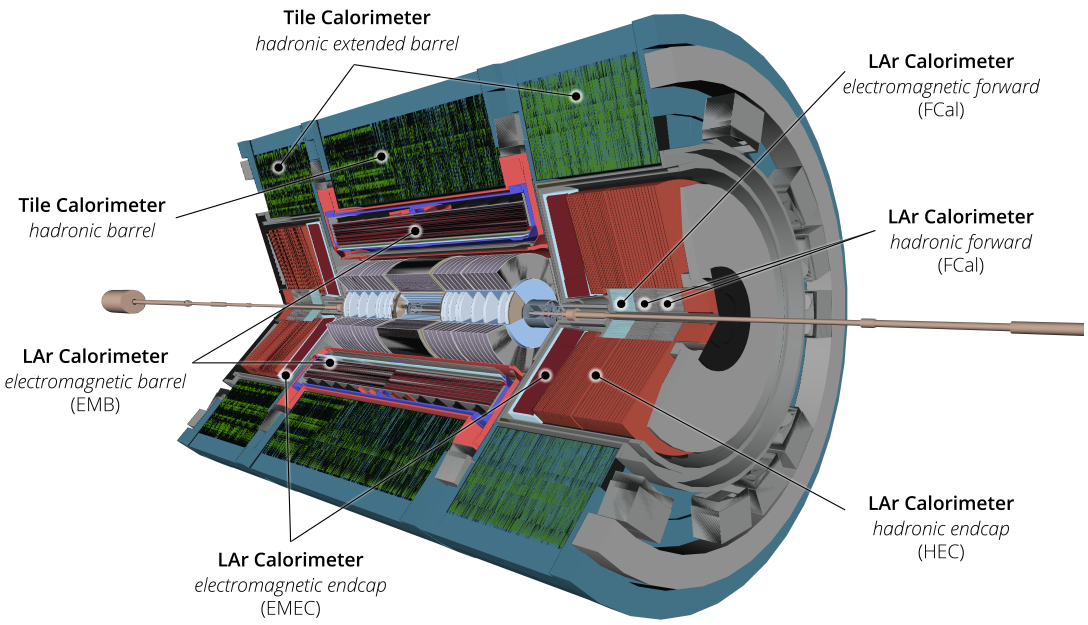

Figure 3: Cut-away view of the ATLAS calorimeter system that measures the energies and positions of charged and neutral particles through interleaved absorber and active layers out to $|\eta| < 4.9$. LAr is used as the active medium for the electromagnetic calorimeters and all of the endcap and forward calorimeters; scintillating Tiles are used for hadron calorimetry in the central region [6].

event can be stored. Thus, a trigger system is implemented to decide which events should be read out and saved for further analysis, while all other data is discarded. It consists of the hardware based Level-1 (L1) Trigger, and the High Level Trigger (HLT) running on external computer components.

The Data Acquisition (DAQ) system transfers and arranges the data from the detector electronics to the offline processing according to the decisions made by the trigger. It is connected to the L1 and HLT levels.

The L1 trigger reduces the frequency of relevant events from 40 MHz to a maximum L1 rate of 100 kHz [6]. Its decisions have to be taken in less than 2.5 μs to avoid overflowing of the readout buffers and the detectors front-end electronics. To achieve this, the calorimeter and muon system signals are processed at reduced granularity. If the event matches certain characteristics, it will lead to the Central Trigger Processor (CTP) sending a L1-Accept (L1A) signal, resulting in a detector readout.

The HLT, which receives this signal, then uses reconstruction algorithms based on the full calorimeter granularity, while also including the muon chambers and inner detectors measurements. The HLT is thus able to reduce the trigger rate to 3 kHz [6] from the previous 100 kHz of the L1 trigger. The relevant events can then be saved for further analyses.

The L1 trigger system, both in its original and updated configuration, is discussed in more detail in Section 3.3.

3.2 Pile-up

In the ATLAS detector, the mean number of interactions that occur in each bunch crossing, the so-called pile-up, can represent a major challenge for the detector sub-systems. Thus, it is useful to introduce a variable describing the pile-up, called the expected pile-up μ [7], which conveys important information on the workload of the detector system.
Pile-up consists of two sources: In-time pile-up and out-of-time pile-up. In the LHC, multiple proton-proton collisions can occur in the same bunch crossing, leading to pile-up collisions in addition to the main interaction vertex of the event. These collisions are called in-time pile-up, which is directly correlated with the instantaneous Luminosity $\mathcal{L}$ by

$$\mu = \frac{\mathcal{L}\sigma_{\text{inelastic}}}{n_c f_{\text{rev}}}, \tag{1}$$

with the number of colliding bunch pairs n_c, the revolution frequency f_{rev}, and the inelastic proton-proton cross section $\sigma_{\text{inelastic}}$ [7].
Out-of-time pile-up is generated by collisions in other bunch crossings due to electronic integration times being larger than the spacing of bunch crossings of 25 ns. This type of pile-up occurs mostly in the calorimetry of the ATLAS detector [7]. Out-of-time pile-up is not considered in the expected pile-up μ [7].

3.3 The Phase-I Upgrade

Between LHC Run-2, which lasted from 2015 to 2018, and Run-3 planned from 2022 to 2025, there was a long shutdown period from 2019 to 2022, during which the ATLAS Phase-I upgrade was installed and commissioned to match the changing proton-proton collision environments due to the LHC upgrades. While the Phase-I upgrade introduces a large number of changes, this thesis will only discuss the changes to the L1Calo trigger system.
In Run-3, the peak instantaneous Luminosity of $\mathcal{L} = 2 \times 10^{34}\text{cm}^{-2}\text{s}^{-1}$ will be achieved for a much longer fraction of each run, which causes a much bigger average pile-up of $\langle\mu\rangle \approx 50$ compared to the average pile-up of $\langle\mu\rangle \approx 30$ in Run-2. The increased pile-up causes great challenges for the detector system, necessitating the use of raised trigger thresholds to reduce the rate to a manageable level.
Thus, the Phase-I trigger upgrade aims to maintain low trigger thresholds by minimising the pile-up impact, which is crucial especially for precision measurements needed for discovering new physics [6].

The L1 Trigger System

An overview of the L1 trigger system in Run-3 is displayed in Figure 4. The new and upgraded parts of the system are highlighted yellow, while the Legacy parts are highlighted in green and blue. It is divided into the Level-1 Calorimeter (L1Calo) and Level-1 Muon (L1Muon) trigger systems, as well as the Level-1 Topological Trigger (L1Topo) and the CTP.
The L1Calo trigger system is responsible for identifying electrons, photons, jets, and τ-leptons, as

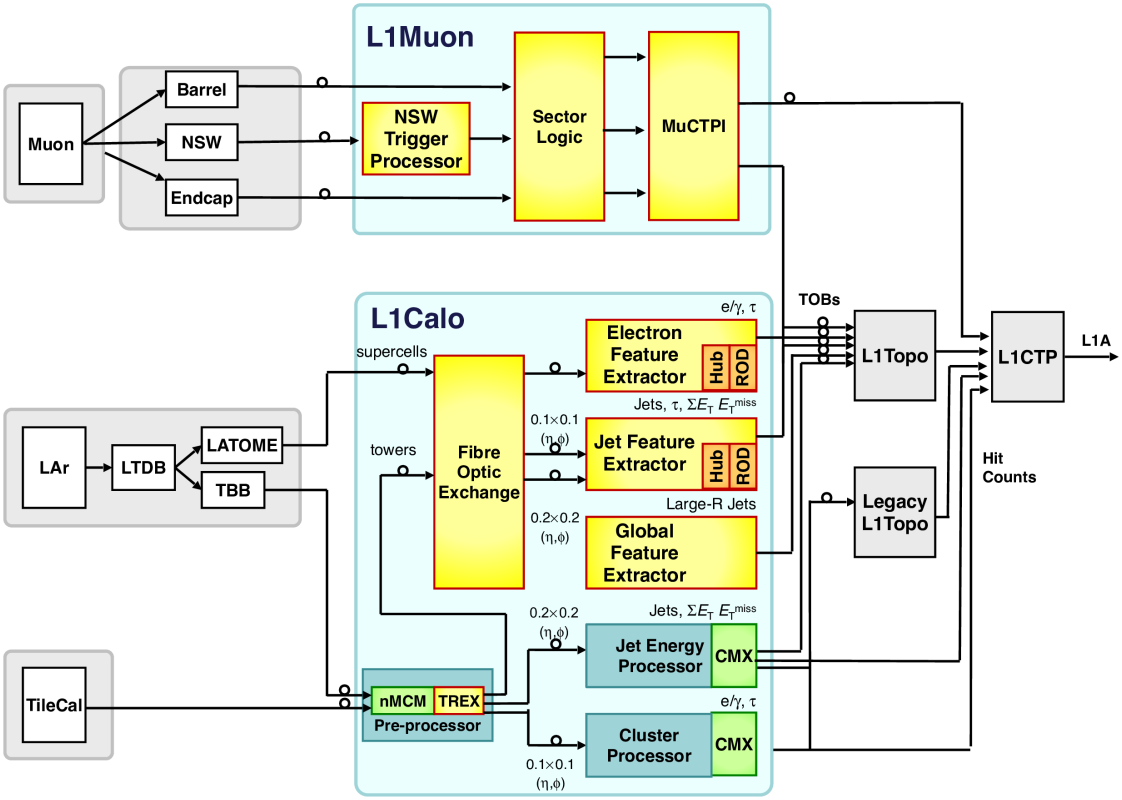

Figure 4: Schematic overview of the L1 trigger system in Run-3. The new and refurbished elements of the L1Muon Phase-I trigger system are shown in yellow. During the commissioning period, both the Legacy (shown in green and blue) and Phase-I L1Calo (shown in yellow) modules are running in parallel [6].

well as events with large missing transverse energy. The L1Muon trigger system is responsible for selecting high-p_T muons. The L1Topo trigger system uses the input Trigger OBjects (TOBs) from the L1Calo and L1Muon trigger systems, which contain information on the transverse energy E_T and $\eta - \phi$ coordinates, and applies topological selections [6]. The purpose of the CTP is to make the final L1A decision, taking information from the L1Calo, L1Muon and L1Topo systems into account. The event is then triggered based on the object type.

The L1Calo Trigger System

The most essential upgrade concerning the L1Calo trigger system during Phase-I is the higher granularity of the LAr calorimeter input information [6]. The more refined processing allows for improved jet identification and rejection against pile-up. Additionally, new jet identification algorithms were implemented, as well as the ability to apply noise cuts and calibration on object level rather than on event-level, which allows for accurate calibration without affecting other global observables in the event such as E_T^{miss}. All of these changes will be highlighted in this section.

The Phase-I system includes several new feature extractor modules responsible for identifying physics objects: The electron Feature EXtractor (eFEX) is able to identify electrons, photons and τ objects in a range of $|\eta| \leq 2.5$ and the full ϕ range, while the jet Feature EXtractor (jFEX)

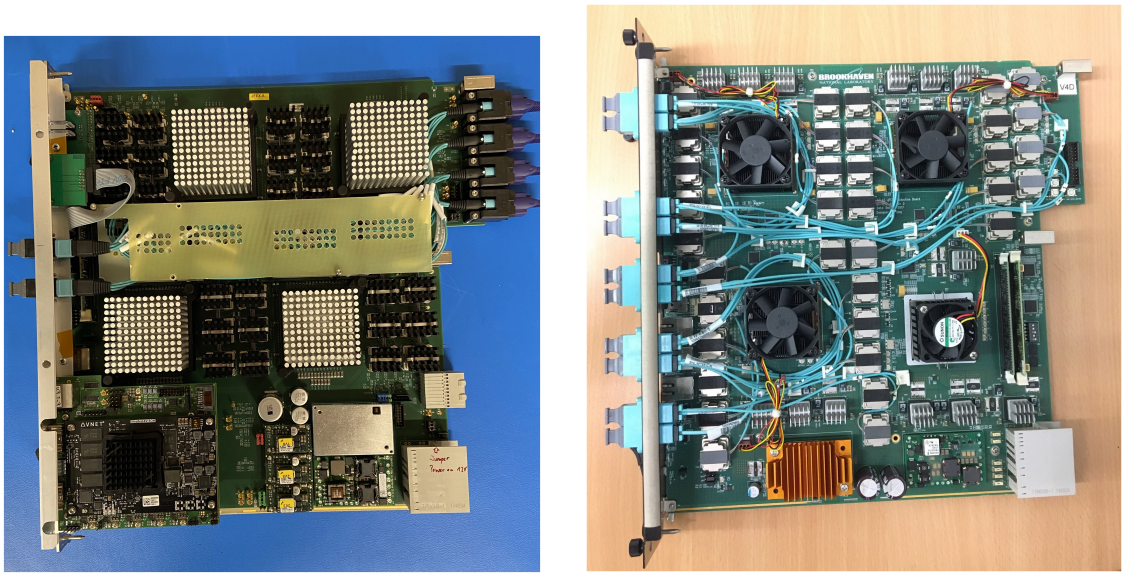

(a) (b)

Figure 5: A production jFEX (a) and gFEX (b) module [6].

uses information in a range of $|\eta| \leq 4.9$ to identify jets, missing transverse energy E_T^{miss} and τ objects. Meanwhile, a third global Feature EXtractor (gFEX) is mainly responsible for identifying large-area (large-R) jets, E_T^{miss} and total transverse energy $\sum E_T$. Modules of the two feature extractors investigated in this thesis, jFEX and gFEX, are shown in Figures 5a and 5b. With the finer input granularity, eFEX uses data with $\Delta\eta \times \Delta\phi = 0.025 \times 0.1$ compared to the input trigger towers of $\Delta\eta \times \Delta\phi = 0.1 \times 0.1$ in Runs 1 and 2 [8]. Similarly, jFEX and gFEX are now provided with calorimeter data of $\Delta\eta \times \Delta\phi = 0.1 \times 0.1$ granularity, compared to the $\Delta\eta \times \Delta\phi = 0.2 \times 0.2$ jet elements used in Run-2 [6].

The Phase-I upgrade made changes to the digitisation process of the input data as well. In Run 2, L1Calo received the input data in analogue format, which was then digitised using the pre-processors [8]. In Run-3 however, L1Calo receives already digitised and calibrated data from the LAr calorimeter, while the input data from the Tile calorimeter is still received in analogue format, digitised by the pre-processors, and transmitted to the FEXs by the new Tile Rear EXtension (TREX) module [6].

The previous Legacy L1Calo trigger is described in more detail in the next section, focusing on jet algorithm.

3.4 The Legacy L1Calo Trigger

The basic architecture of the Legacy L1Calo trigger is shown in Figure 6. The analogue trigger-tower input coming from the calorimeters is digitised in the Pre-Processor [8]. Additionally, it applies a filtering technique to improve the signal-to-noise ratio, and associates each pulse with a bunch crossing. Using a Look-Up Table (LUT), the signals are then calibrated, the pedestal is subtracted, noise is suppressed, and problematic channels are turned off [8].

The identification of object candidates is done in the two algorithmic processors. The Cluster

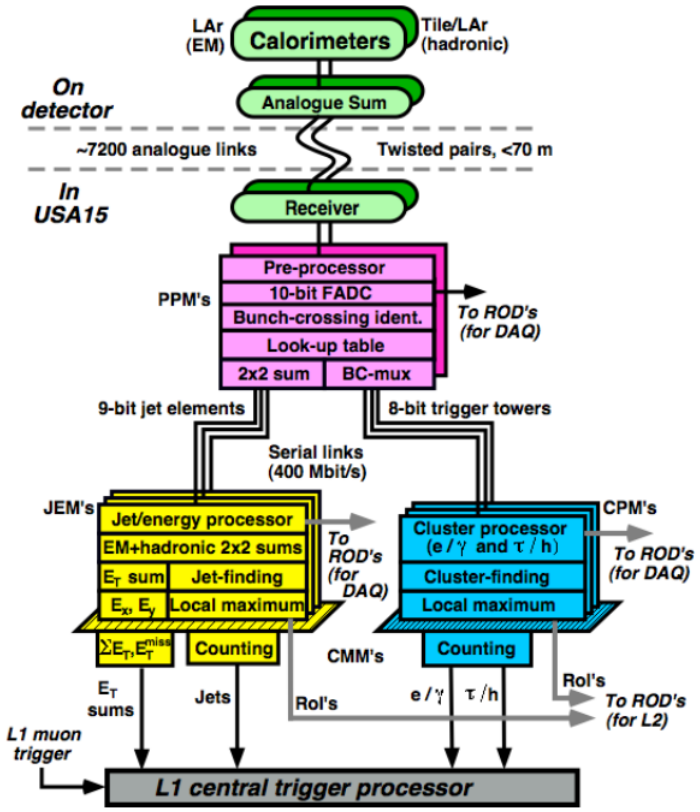

Figure 6: Architecture of the Legacy L1 Calorimeter Trigger [8].

Processor (CP) is responsible for electrons, photons and τ with high transverse energy [8]. It services a region of $|\eta| < 2.5$, which is where the ID coverage ends. The Jet/Energy-sum Processor (JEP) identifies jets and produces the global sums of total E_T, missing E_T and jet-sum E_T [8] and operates in $|\eta| < 4.9$. The jet trigger however only extends up to $|\eta| < 3.2$ at the limit of endcap acceptance [8], which is a crucial difference compared to the Phase-I system. As mentioned in the previous section, the CP operates on $\Delta\eta \times \Delta\phi = 0.1 \times 0.1$ granularity in the central regions, while the JEP works with so-called jet elements, corresponding to a granularity of $\Delta\eta \times \Delta\phi = 0.2 \times 0.2$. In the forward regions of the calorimeter, the input granularity becomes coarser [8].
All the information on identified objects and energy sums is then sent to the CTP and L1Topo. The CP consists of four crates, each holding 14 Cluster Processor Modules, handling one calorimeter quadrant. The JEP is made up of two crates, with 16 Jet/Energy Modules each [8].

The Legacy Jet Algorithm

The Legacy jet algorithm works by summing the transverse energy E_T in so-called trigger tower windows as shown in Figure 7. These windows consist of 4×4 jet elements, corresponding to 0.8×0.8 in granularity [8]. The window E_T sums are then compared to a 10-bit energy threshold. Since it is possible for a jet to exceed the threshold in multiple windows, these duplicate hits

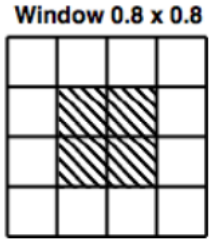

Figure 7: Jet trigger algorithm window, based on jet elements of 0.2×0.2 [8].

are removed by requiring an inner 2×2 region to be the local maximum relative to its eight overlapping nearest neighbours [8]. In total, eight different jet thresholds are implementable.

3.5 The Jet Feature Extractor (jFEX)

The jFEX system consists of six jFEX modules: four covering the central region of the calorimeter, and two using information from the forward region [6]. As mentioned before, jFEX works with a granularity of $\Delta\eta \times \Delta\phi = 0.1 \times 0.1$ in the central regions. In the forward regions, the granularity becomes coarser and η dependent.
Each jFEX module has four processor Field Programmable Gate Arrays (FPGAs), each covering a so-called core region, corresponding to $\Delta\eta \times \Delta\phi = 0.8 \times 1.6$ in the barrel region, or $\Delta\eta \times \Delta\phi = 3.3 \times 1.6$ in the Endcap and Forward regions.
Some objects, such as large-R jets, can leave energy deposits that overlap the boundary of a single FPGA core area. Thus, additional information from the neighbouring environment is included to correctly identify large objects [6].

Pile-up Subtractions and Noise Cuts

Before the different algorithms are applied, the input data first undergoes a series of pile-up subtraction and noise cuts [6]. First, the energy of each trigger tower is corrected for pile-up: Each energy value is weighted, and all energy values within a configurable threshold are summed up. These sums are made separately for different calorimeter regions. For each region sum, the average is calculated and subtracted from each trigger tower energy, yielding the final pile-up subtracted energy [9].
In 2023 data taking, noise cuts are set to 1 GeV for trigger towers in LAr, 0.5 GeV in the Tile Calorimeter, and 0 GeV in the FCal [10]. The jFEX noise cuts in comparison to the legacy noise cuts implemented in the CTP LUT can be found in Figures 8a and 8b for the EM and HAD layers respectively. The 1 GeV noise cuts applied in LAr can be found at the beginning of the EM layer, and in the HAD layer after the end of the Tile calorimeter. While Tile covers a total range of $|\eta| < 1.7$, only the trigger towers in $|\eta| < 1.4$ are used for the L1 trigger decision, as the LAr information from the HEC is used in the overlapping region. While jFEX noise cuts are nominally set to 0.5 GeV in the Tile region, these noise cuts are being overwritten by the higher noise cuts set in the L1Calo Pre-Processor for Tile, which the Tile input data is transmitted from. Thus, the 0.5 GeV noise cuts do not correspond to the actual noise cuts applied to the Tile trigger

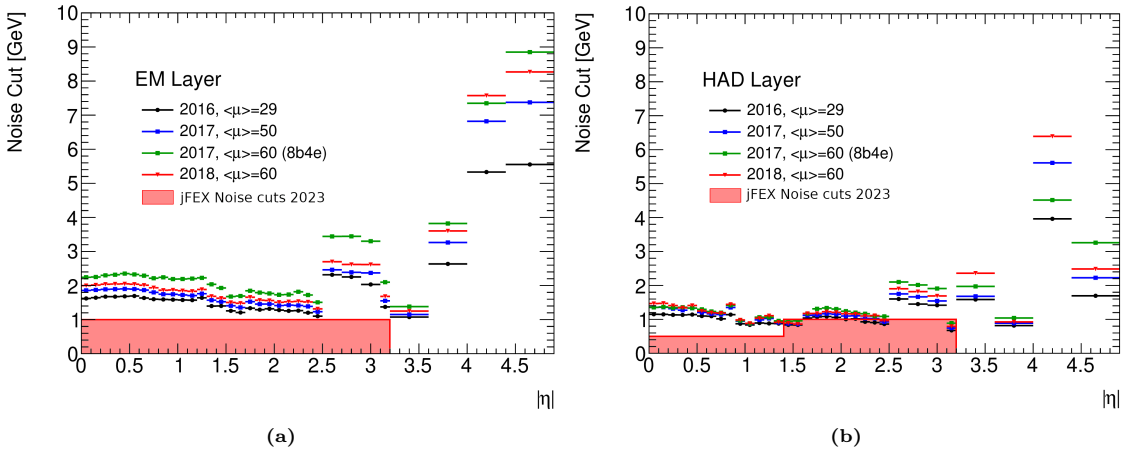

Figure 8: Legacy CTP noise cuts used during Run-2 for the EM-layer (a) and the HAD-layer (b) taken from [11] compared to the jFEX noise cuts used in 2023 data taking as a function of Pseudorapidity $|\eta|$.

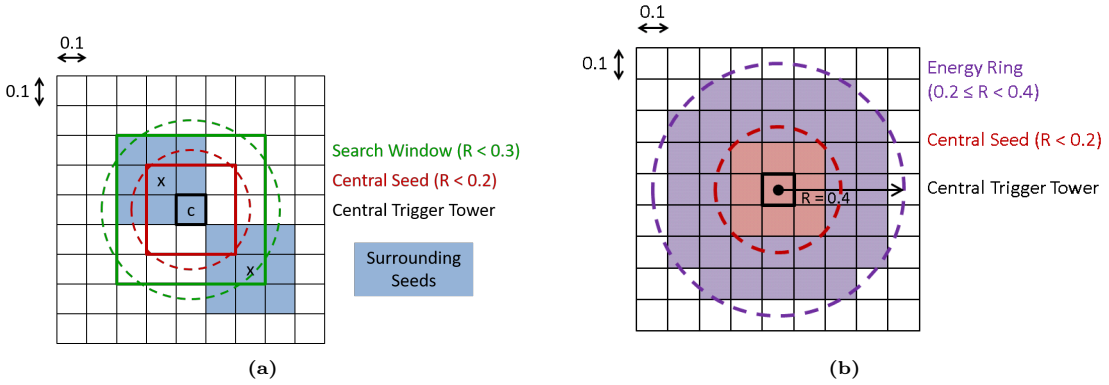

Figure 9: (a) The seeding process by which local maxima are identified in the jFEX. (b) A small-radius jet as defined by the jFEX [6].

towers.

jFEX Small-R Jet Algorithm

Similar to the Legacy jet algorithm, the jFEX small-R jet algorithm is based on the Sliding Window Algorithm [6]. In a window of 0.3×0.3, corresponding to $R < 0.2$, the energies are summed, forming so-called seeds as shown in Figure 9a. It is expected that the majority of the jet energy is located inside of its seed. Then, seeds inside of a 0.5×0.5 search window, equivalent to $R < 0.3$, are compared to find the local maximum. The seed with the largest energy sum is chosen, with the central tower of the seed as the jet centre. The final jet energy consists of the energy in the central seed with $R < 0.2$, as well as the energy of a ring $0.2 < R < 0.4$, as seen in Figure 9b. As opposed to the Legacy jet algorithm, the tower regions considered for the jet energy are round.

jFEX Jet E_T Calibration

While jets were calibrated with all other physics objects in the CTP in the Legacy system, jet calibration can now be applied directly in jFEX. In total, 54 different calibration parameters are used, depending on E_T and η [9].

3.6 The Global Feature Extractor (gFEX)

In contrast to jFEX, which consists of many modules, each covering a slice of the ATLAS detector, gFEX is designed to process the entire event on only one board. This approach is beneficial for identification of global observables, such as E_T^{miss}, or large objects that could cross the boundaries of a single module in other systems, such as large-R jets [6]. In total, three processing FPGAs are located on the gFEX board, two covering the central regions $|\eta| \leq 2.5$, and one responsible for the forward regions. Every FPGA covers 2 regions of $6 \times 32 = 192$ trigger towers in total.
While the main purpose of gFEX is not the identification of small-R jets, gFEX is nevertheless studied for single-jet performance in this thesis.

gFEX Small-R Jet Algorithm

The input from the LAr and Tile calorimeters with 0.1×0.1 granularity is summed up into so-called gTowers, with 0.2×0.2 granularity in the barrel region [6]. Jets are then identified using gBlocks, which are groups of 3×3 gTowers, corresponding to $R < 0.3$ jets. The energy of all gTowers in a gBlock is summed up to the jet energy.
For every 6×32 trigger tower region, the two highest gTowers are sent to L1Topo, resulting in 4 per FPGA and thus 12 gTowers in total [9].

4 Building the Framework

The proton-proton collision events are characterised by the signatures of the final state particles in the different subdetectors. By analysing the available tracking information and recorded energy deposits, final state particles are reconstructed using software level reconstruction algorithms [12, 13]. In contrast to the L1 TOBs, the so-called offline objects retrieved from reconstruction are obtained using the full granularity input. Yet, several processing steps have to be applied on the offline objects in order to accurately determine the trigger performance. This includes background corrections for jets known as cleaning, further energy calibrations for electrons and jets, as well as overlap removal.

4.1 Jet Cleaning

After the reconstruction process, the set of offline jets does not only contain the desired jets produced from proton-proton collisions, but also reconstructed jets from several background origins [14]. These reconstructed jets from background processes are called fake jets, with three sources being the main contributors [14]:

- When protons diverge from from the proton beam upstream of the collision point, their interactions with the collider material may produce muons, reaching the detector and producing energy depositions. These energy depositions can be reconstructed as jets with relatively high energy, contributing to the aforementioned fake jet background.
- Another source of fake jets are muons created in cosmic ray showers in the atmosphere. These muons can enter the detector and produce a fake jet in a similar way as the beam induced background.
- The third main source of fake jets is due to sporadically noisy cells in the calorimeter. Most events with large amounts of calorimeter noise are already removed in advance, yet a small residue needs to be rejected in the cleaning process.

In order to identify the good jets from the entire set of offline jets, a set of criteria needs to be applied to distinguish between the two different types. This process is known as jet cleaning, and the jet quality variables used by ATLAS are summarised in the next section.

Jet Quality Variables

The selection criteria are based on several discriminating variables, which can be divided into pulse shape variables, energy ratio variables, and track-based variables [14].
Pulse shape variables are based on the signal pulse shape in the LAr calorimeters, and they are useful to discriminate from LAr calorimeter noise. They are mainly based on the quadratic difference $Q_{\text{cell}}^{\text{LAr}}$ between the expected pulse shape from electronics response and the actual pulse shape. This cell-based quantity is used to derive the average jet quality $\langle Q \rangle$, which is defined as the energy-squared weighted average of $Q_{\text{cell}}^{\text{LAr}}$ of all the cells in the jet [14].
Additionally, it is useful to examine the total energy of all LAr calorimeter cells belonging to a jet. The fraction of this energy with a poor signal shape quality ($Q_{\text{cell}}^{\text{LAr}} > 4000$) is defined as

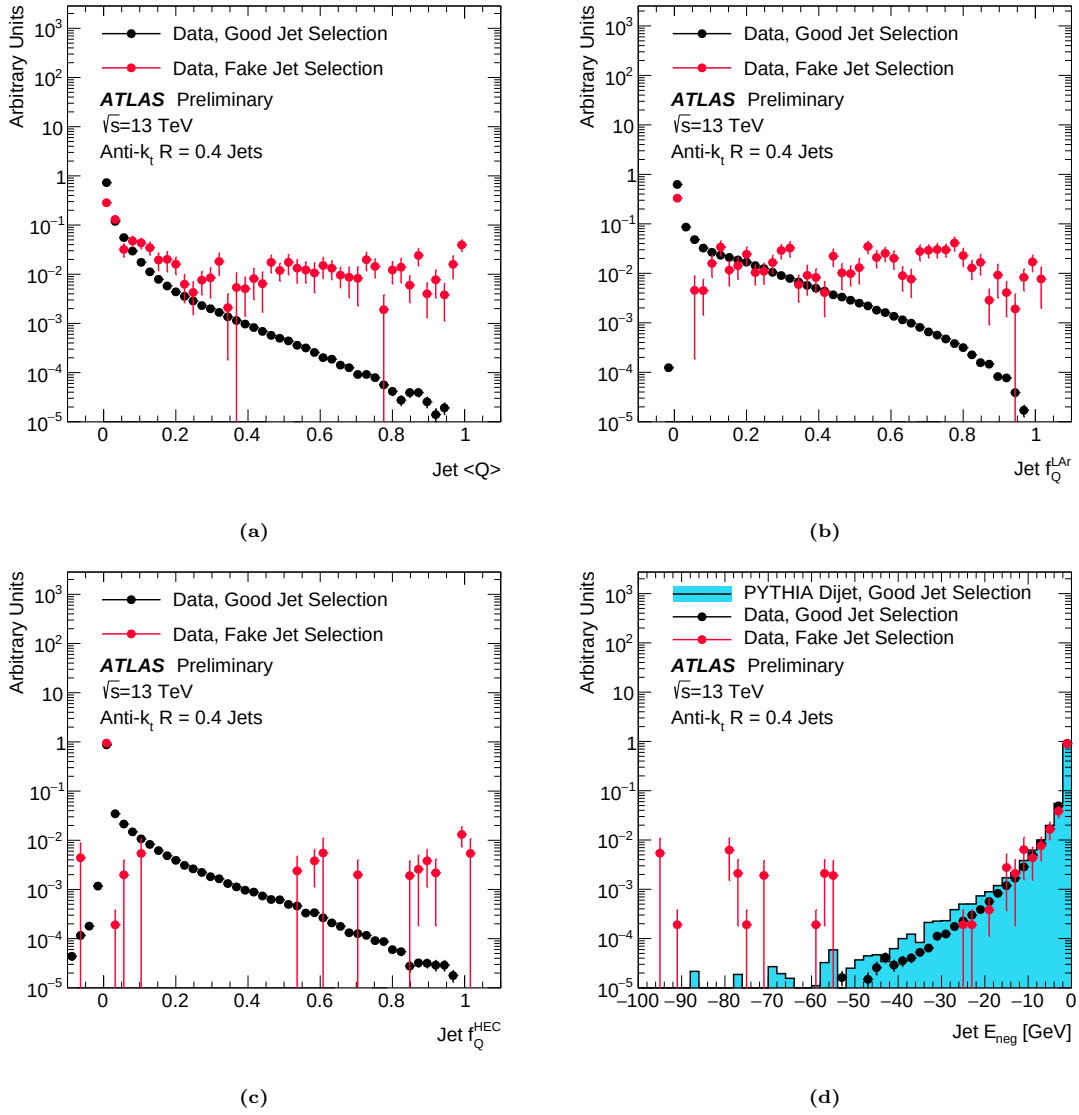

Figure 10: Distributions of f_Q^{LAr} (a), f_Q^{HEC} (b), $\langle Q \rangle$ (c) and E_{neg} (d) in good jets enriched sample data (black points) and simulation (blue histogram) only shown for (d). Distributions from fake jet enriched samples are superimposed (red points) [14].

f_Q^{LAr}. Similarly, f_Q^{HEC} is defined as the fraction of energy of all cells in the hadronic calorimeter belonging to a jet with $Q_{\mathrm{cell}}^{\mathrm{LAr}} > 4000$. Finally, it is possible to make use of the fact that sporadic calorimeter noise can generate negative energy deposits by defining the energy sum of all cells with negative energy E_{neg}.

$\langle Q \rangle$, f_Q^{LAr} and f_Q^{HEC} show a large number of good jets at zero, while the fake jets tend to produce higher values [14] as shown in Figures 10a to 10c using data with a good jet and a fake jet selection respectively [14]. This effect is used to discriminated fake jets from good jets. For E_{neg}, most jets have values of $|E_{\mathrm{neg}}| < 50$ GeV, with a fake jet population of outliers with $|E_{\mathrm{neg}}| > 60$ GeV as seen in Figure 10d [14].

Energy ratio variables make use of the increased localisation in longitude of fake jets due to

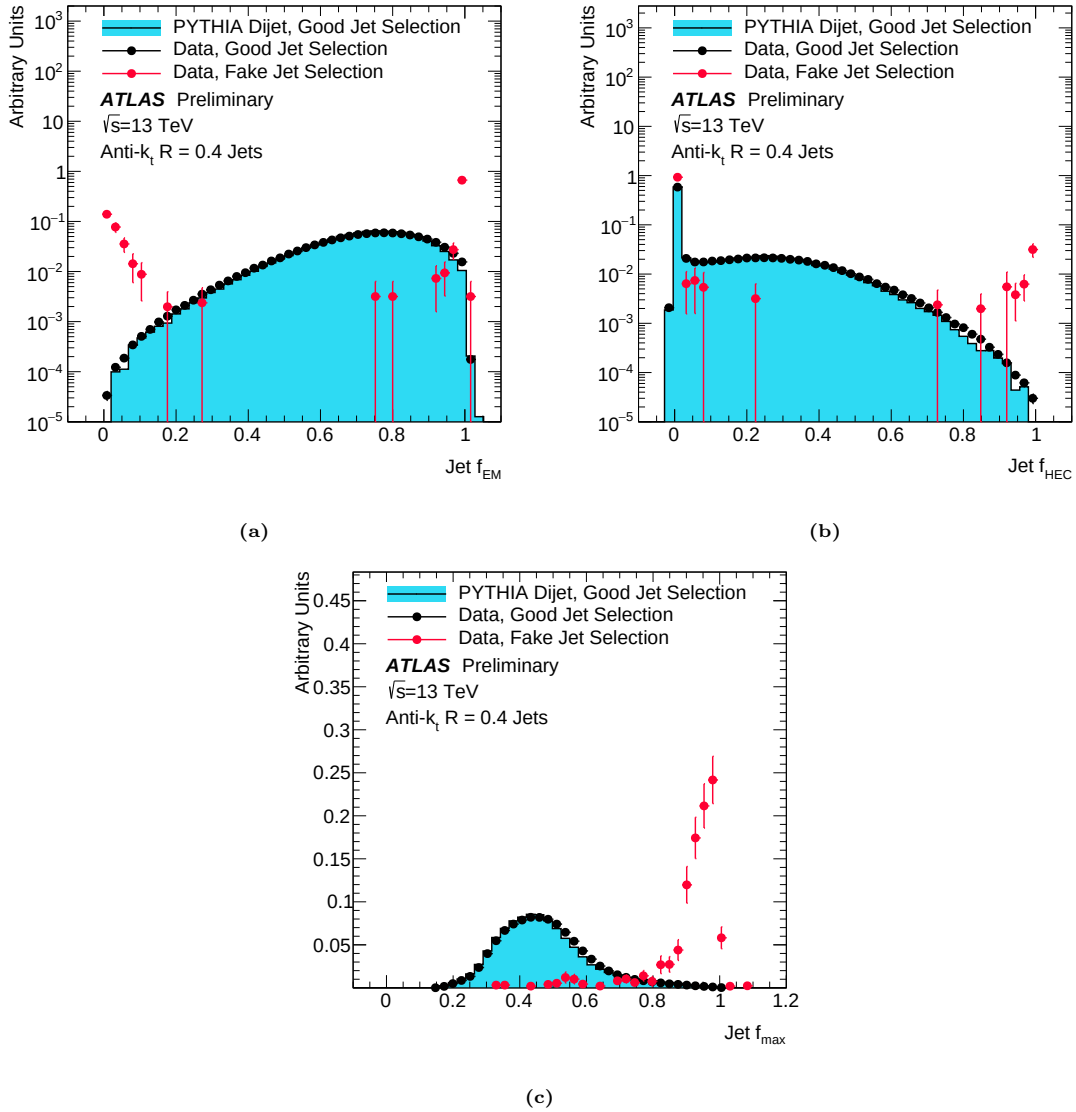

Figure 11: Distributions of f_{EM} (a), f_{HEC} (b) and f_{max} (c) in the good jets enriched sample for both data (black points) and the simulation (blue histograms). Distributions from the fake jet enriched samples are also superimposed (red points) [14].

beam-induced background and calorimeter noise. The corresponding quality variables are the electromagnetic fraction f_{EM}, which is defined as the ratio of energy deposited in the electromagnetic calorimeter to the total energy of the jet, as well as the hadronic energy fraction f_{HEC} which is defined analogously with the hadronic calorimeter. Additionally, the maximum energy fraction in any single calorimeter layer f_{max} is used [14].

All three variables show smooth distributions for good jets, while f_{EM} and f_{HEC} tend to be either very low or very high for fake jets. Similarly, fake jets seem to produce very high values of f_{max} [14]. The corresponding distributions are shown in Figures 11a to 11c.

The **track based variables** use track information from the inner detector, since charged hadrons from real jets leave tracks in the ID, while fake jets from muons or calorimeter noise do not. Since

1.	$f_{\text{HEC}} > 0.5$ and $\lvert f_Q^{\text{HEC}} \rvert > 0.5$ and $\langle Q \rangle > 0.8$
2.	$\lvert E_{neg} \rvert > 60$ GeV
3.	$f_{\text{EM}} > 0.95$ and $f_Q^{\text{LAr}} > 0.8$ and $\langle Q \rangle > 0.8$ and $\lvert \eta \rvert < 2.8$
4.	$f_{\text{max}} > 0.99$ and $\lvert \eta \rvert < 2$
5.	$f_{\text{EM}} < 0.05$ and $f_{\text{ch}} < 0.05$ and $\lvert \eta \rvert < 2$
6.	$f_{\text{EM}} < 0.05$ and $\lvert \eta \rvert \geq 2$

Table 1: Selection criteria for the BadLoose working point of the Jet Cleaning Tool [14]. If at least one of these criteria is met, the jet is identified as a BadLoose jet.

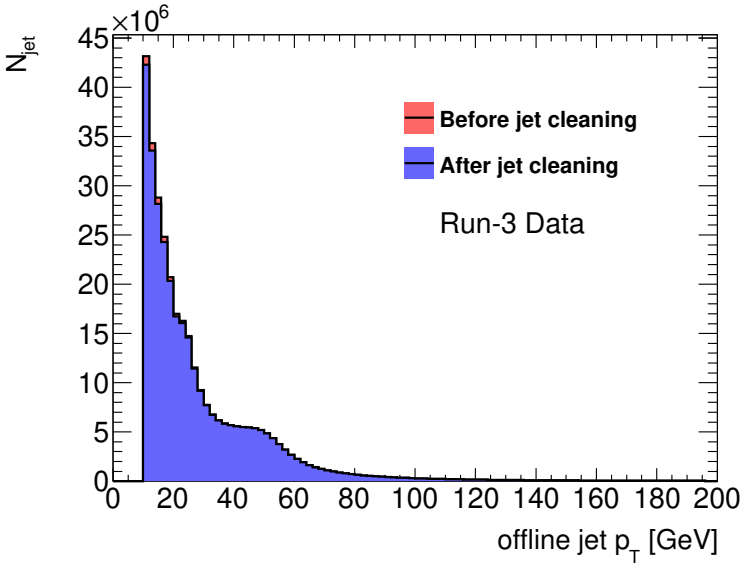

Figure 12: Offline jet transverse momentum distribution in Run-3 data after (blue) and before jet cleaning (red).

track based variables are only used for a tighter selection, they will not be covered here, as they are not required for the loose selection used in this analysis.
All of the jet quality variables introduced in this section are used to define six selection criteria for the BadLoose working point. This working point, and its effect on the jets in the analysed data set will be described in the following section.

Implementation and Effects

Jet cleaning is implemented using the Jet Cleaning Tool provided in Athena, the ATLAS software repository [15]. The BadLoose working point was selected to maintain a high good jet efficiency, while still rejecting fake jets reliably. A jet is identified as a fake jet at the BadLoose working point if it satisfies at least one of the criteria listed in Table 1. Correspondingly, a jet is identified as a loose jet if it is not flagged as a BadLoose jet.
The effect of the jet cleaning on the data set can be observed by plotting the offline jet p_T distribution before and after the jet cleaning as seen in Figure 12. The effect of jet cleaning on the data sample is rather small, with only few jets at low energies being flagged as fake jets. The small effect is largely explained by the previous cleaning during the reconstruction process. The

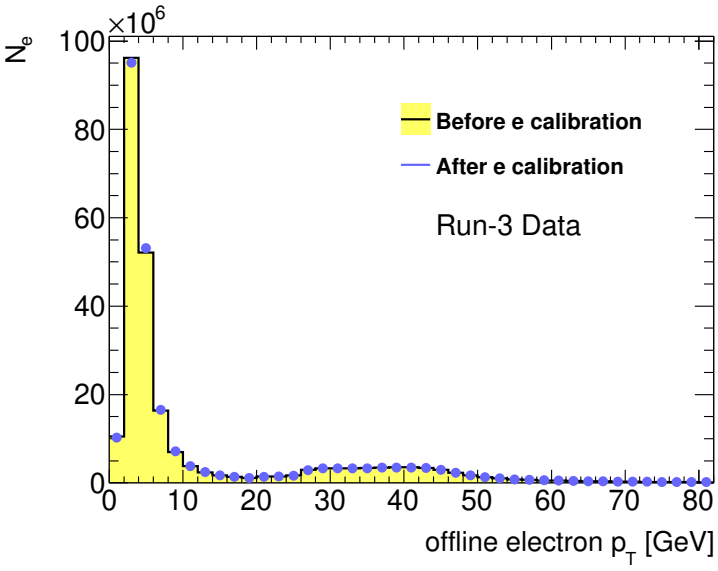

Figure 13: Offline electron transverse momentum distribution in Run-3 data after (yellow) and before jet cleaning (blue).

10 GeV cut visible in the distribution is set in the preselection by ATLAS due to the minimum threshold for calibration.

4.2 Electron Calibration

During the reconstruction, an initial calibration is applied to the offline electrons. However, precise analysis requires an improved calibration of electrons and jets [16]. Accordingly, the necessary electron calibration tool is implemented in Athena, performing the following steps for an improved energy calibration [16]:

- First a correction is applied to the data accounting for relative energy scales in different EM calorimeter layers.
- Then, the electron energy is estimated from the calorimeter energy deposits using an algorithm trained on simulated data, with the goal of improving energy resolution and correcting for energy lost in the material upstream of the calorimeter.
- Another correction is applied taking local non-uniformities in calorimeter response into account, with an additional adjustment due to the overall energy scale in the data.
- Finally, the resulting calibration is checked by using an independent sample in data and simulation, and comparing the two results.

These calibration steps were included in this framework and applied to the data. The effect on the electron p_T distribution can be seen in Figure 13. The effect on the data is very small, with only very low energy electrons in the first and second bin experiencing a significant change in

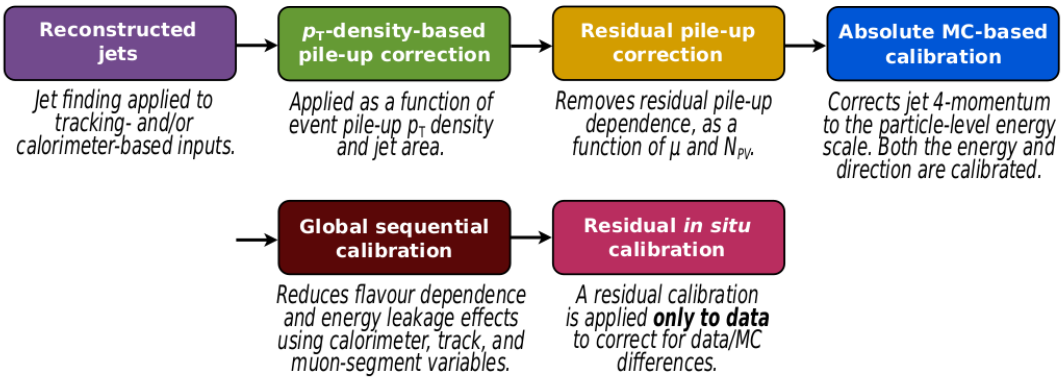

Figure 14: Stages of jet energy scale calibrations. Each one is applied to the four-momentum of the jet [17].

momentum. Since electrons at low p_T benefit most from the improved energy resolution, they are affected the most by the calibration.

4.3 Jet Calibration

Similarly to electrons, jets are calibrated in this framework using the jet calibration tool implemented in Athena. As part of the jet energy scale (JES) calibration, several correction are applied to the jet four-momentum, an overview of which can be seen in Figure 14.

- First a correction accounting for excess energy from in-time and out-of-time pile-up is applied [17]. This correction consists of two parts, one based on jet area A and p_T density, and the other targeting residual jet p_T dependence on pile-up activity as a function of pile-up μ and the number of reconstructed primary vertices in the event N_{PV}.
- Next, the absolute JES calibration adjusts jet energy and direction to agree with the energy scale of Monte-Carlo simulated di-jet events [17].
- The global sequential calibration uses calorimeter, tracking and muon chamber information to remove dependence on specific observables related to differences in quark- and gluon-initiated jets, and energy distribution of the constituent particles [17].
- Similarly to the electron procedure, a final residual *in situ* calibration is applied based on the ratio of jet response in data and Monte-Carlo simulation [17].

The effect of jet calibration on the data in this analysis is depicted in Figure 15.
As also seen in the electron calibration, jet calibration affects low p_T jets significantly more, due to pile-up effects being more prevalent at low energies.

4.4 Overlap Removal

In general, offline objects reconstructed from particle signatures are not mutually exclusive. For example, an electron can be reconstructed as a jet as well, as both provide hits in the ID and energy deposits in the calorimeters. While analysing the amount of jets in the selected events, the

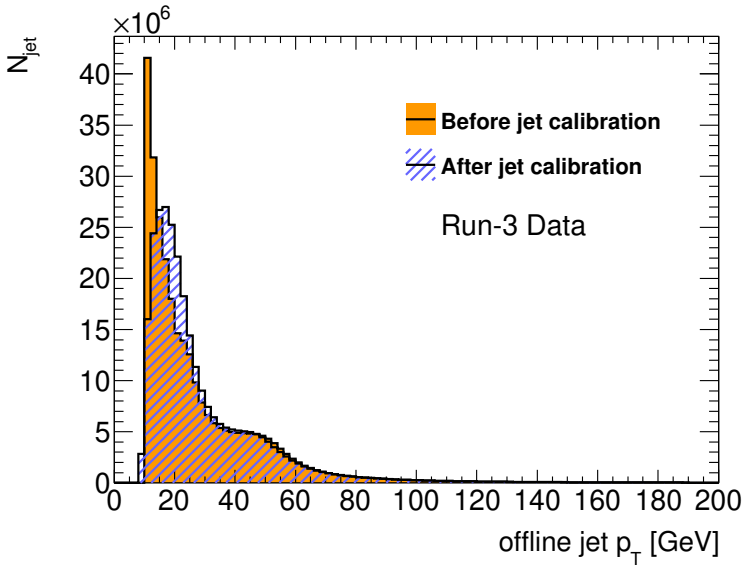

Figure 15: Offline jet transverse momentum distribution in Run-3 data after (blue) and before jet calibration (orange).

majority of events include two or more jets, with only a handful of events containing one or zero jets, as seen in Figure 17. This suggests that there are more offline jets in the data than expected, which could be explained by the aforementioned duplicate reconstruction. To solve this problem, overlap removal (OR) is included in this framework:

The suspicion that electrons in the selected events were also reconstructed as jets can be investigated by analysing geometric correlations between the two leading electrons and the two leading jets. Accordingly, the distance in the η-ϕ-plane $\Delta R = \sqrt{(\Delta\eta)^2 + (\Delta\phi)^2}$ is plotted as a distribution. The result can be seen in Figures 16a to 16d. Evidently, there is a high correlation between the leading electron and the leading jet, with the overwhelming majority of events showing a ΔR around zero. Similarly, the correlation between the sub-leading electron and the sub-leading jet is clear. When comparing the leading jet to the sub-leading electron, or the sub-leading jet to the leading electron, there are also clear correlations visible, yet the objects are either perfectly aligned ($\Delta R = 0$) or perfectly opposite ($\Delta R \approx \pi$) in half of the events respectively. This confirms the suspicion that an overlapping reconstruction has taken place, likely concerning the two leading jets, since no correlation is apparent after the sub-leading jet.

The overlap removal is done using the Overlap Removal Tool implemented in Athena. The standard working point, which was used in this thesis, applies the removal rules for electrons and jets displayed in Table 2. The cuts in this working point are based on the size of reconstructed jets, which use an input of $R = 0.4$ in the reconstruction algorithm.

Reject	Against	Criteria
jet	electron	$\Delta R < 0.2$
electron	jet	$\Delta R < 0.4$

Table 2: Removal criteria for the standard working point of the Overlap Removal Tool [18].

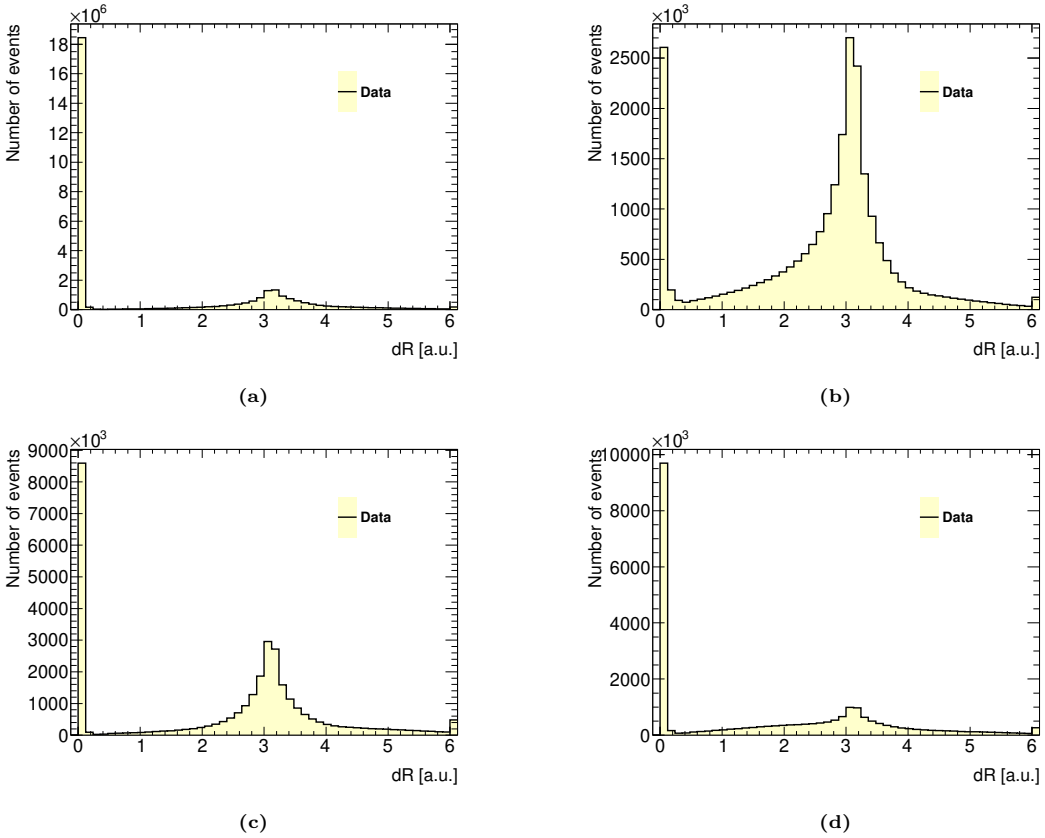

Figure 16: ΔR distribution between (a) leading jet and leading electron, (b) leading jet and sub-leading electron, (c) sub-leading jet and leading electron, (d) sub-leading jet and sub-leading electron.

With the overlapping physics objects removed, the number of jets in the event has decreased as expected, as seen in Figure 17. Compared to before the overlap removal, the distribution seems to have shifted to the left by approximately two jets, which is in agreement with the expectation that the two leading electrons were also reconstructed as jets, with the two leading jets being removed in the overlap removal. In total, the number of events containing jets decreases as well, since many jets are removed from the events.

To confirm that the overlap removal has worked as intended, the ΔR correlations after the overlap removal, as seen in Figures 18a to 18d, can be examined. All plots show the same random characteristics, with no entries in the $\Delta R = 0$ region, proving that the overlap removal has eliminated the correlations between jets and electrons.

With the remaining jets cleaned and calibrated, and not containing any electron duplicates, the jet efficiencies can be calculated accurately.

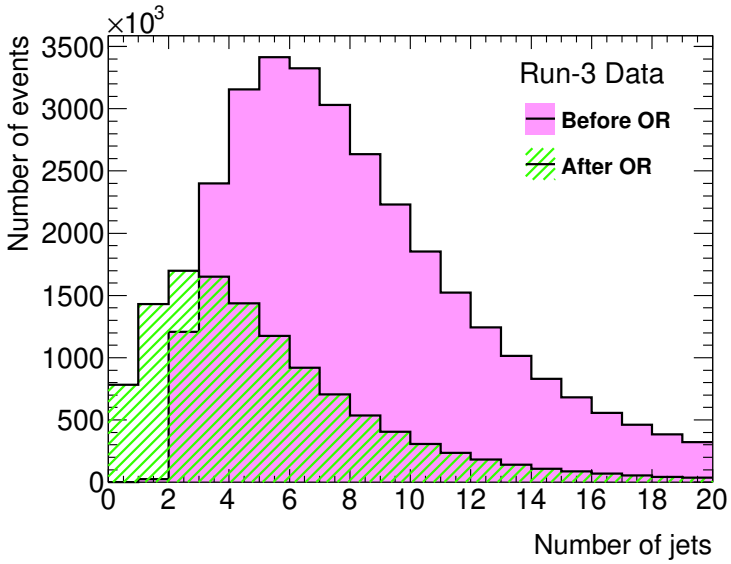

Figure 17: Amount of jets before and after overlap removal in Run-3 data.

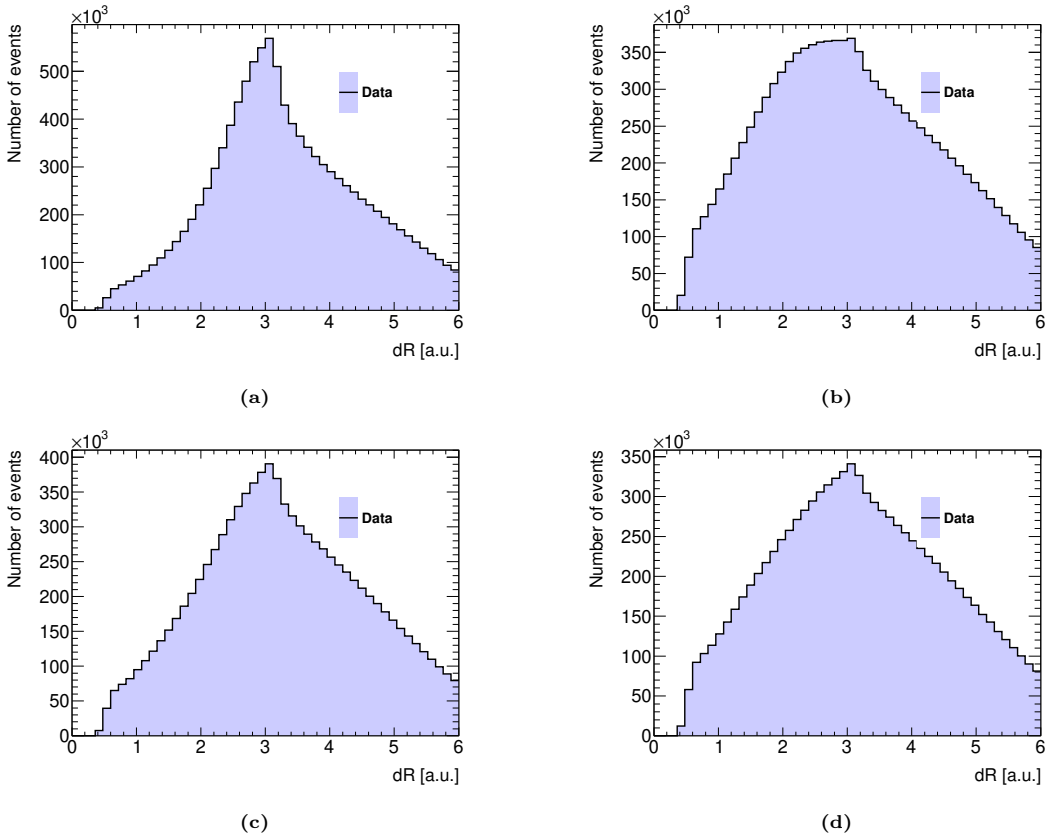

Figure 18: ΔR distribution after OR between (a) leading jet and leading electron, (b) leading jet and sub-leading electron, (c) sub-leading jet and leading electron, (d) sub-leading jet and sub-leading electron.

5 Level-1 Single-jet Trigger Efficiencies

In this section, the concept of trigger efficiencies is discussed in detail. The efficiency calculation strategy is described, including a Z boson selection and the tag-and-probe method. In the last step, the behaviour of the L1 trigger is emulated and the resulting object-level jet trigger efficiencies are analysed.

5.1 Trigger Efficiencies

The L1 trigger efficiency quantifies the correct identification of TOBs above the threshold of a trigger by comparing offline and TOB information. If a TOB lies above the threshold energy E_{th} and is thus triggered, the corresponding object is assigned efficiency $\varepsilon = 1$. Similarly, if a TOB does not pass the energy threshold, it is assigned efficiency $\varepsilon = 0$.
The reduced granularity of the input data compared to the offline information obtained from reconstruction leads to an energy resolution effect. The TOB extracted by the L1 trigger will in many cases have a deviating energy from the offline energy of the physics object. This deviation is distributed approximately Gaussian around the offline energy, with non-Gaussian detector effects appearing in the tails of the distribution.
As this thesis targets L1 jet trigger efficiencies, an example using a single-jet trigger with $E_{th} = 40$ is given: For very low offline jet energies, the efficiency is expected to be zero, as the offline energy is far below the threshold energy. Similarly, for high offline jet energies, the efficiency is expected to be equal to 1. In the region around the threshold energy, the resolution effects comes into effect. An offline jet with $E > E_{th}$ may produce a TOB with $E < E_{th}$, resulting in some TOBs having efficiency $\varepsilon = 1$ instead of zero. Thus, the average efficiency lies somewhere between 0 and 0.5 to the left of E_{th}, and between 0.5 and 1 on the right side, where the TOB energies are occasionally underestimated. Hence, the trigger efficiency as a function of offline jet transverse momentum p_T is approximately described by a Gaussian error function, being the antiderivative of the Gaussian energy resolution. The example is shown in Figure 19. Note that threshold energies are usually given without a unit, since trigger thresholds are not necessarily calibrated towards offline jet energies.

5.2 Object-level and Event-level Efficiencies

Two different types of efficiencies have to be distinguished: Object-level efficiencies are described by the scenario above, where every TOB and offline jet is considered in the efficiency calculation. This type of efficiency focuses on the ability of the trigger system to correctly identify TOBs above its trigger threshold.
The second type of efficiencies are event-level efficiencies. For event-level efficiencies, the efficiency is calculated for every event instead of every offline jet. For example, for the single jet trigger from the example above (L1_J40) an event would be considered efficient if at least one TOB would be identified above the trigger threshold of 40. The correct identification of the remaining offline jets in the event would be irrelevant. Thus, event-level efficiencies focus on the triggers purpose to send L1 accepts based on a single criterion, rather than correct functionality of the feature extractor modules.

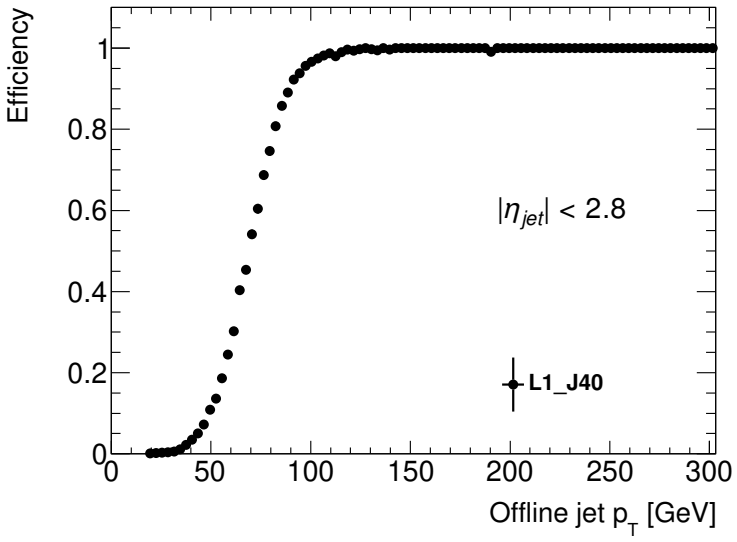

Figure 19: L1_J40 Legacy jet trigger efficiency in Run-3 data. The trigger name contains the trigger level (L1), as well as the trigger criterion (A single jet with TOB energy above x → Jx).

The single-jet efficiencies calculated in this thesis are object-level efficiencies, taking the correct identification of every TOB into account, while multi-jet efficiencies are naturally event-level efficiencies.

5.3 Efficiencies using Z Boson Events

There are several important criteria for an optimal event regarding jet efficiency calculations:

- First, there should be a large enough amount of jets in the events, so there is no need for an enormous amount of data to be processed in order to reach good statistics. Thus, when choosing a type of event that can occur in a proton-proton collision, selecting one with a high cross section for higher order processes including jets is advantageous.

- Secondly, the events should be easy to select by having clearly identifiable physics objects in the final state, such that simple event selection cuts can be performed.

- Finally, there should be other physics objects in the event that are able to fire a trigger. These objects can be used as so-called tag objects in the tag-and-probe method, which is an efficiency calculation method discussed in the next section.

As covered in Section 2, Z boson events suffice all these criteria: They show a high cross section for jets in the next to leading order process, the Z boson can be selected using a series of simple cuts, and the two leading electrons are available as tag objects.

5.4 The Tag-and-Probe Method

The tag-and-probe method is a common method to calculate efficiencies by obtaining a clean and unbiased set of jets [19]. First, a set of criteria is applied to the tag object. In this analysis, the two leading electrons, and thus the Z boson they originate from, is used as a tag. In this case, the criteria correspond to a Z boson selection, which ensures that the tag objects stem from the desired Z decay.
If the tag objects pass all selection criteria, the remaining probe objects in the event likely originate from a Z decay as well. Thus, the remaining jets can be used as probe jets for the efficiency calculation.
The tag-and-probe method circumvents a specific bias that can occur in trigger efficiencies: Since all events in a data set were triggered by a trigger, it is possible that some of the events used to determine the trigger efficiencies were triggered by the very trigger the efficiency is designed to analyse. These cases can bias the efficiency towards higher values. Through the criteria applied to the tag electrons the tag-and-probe method ensures that the event was triggered by an electron trigger, which avoids this bias for jet trigger efficiencies.

5.5 Event Selection

While the data used for this analysis already contains a preselection for Z bosons and already contains the desired $Z \to e^+e^-$ events, other decays such as $Z \to e^+e^-\gamma$, $Z \to \mu^+\mu^-\gamma$ and $Z \to e^\pm fe^\mp$ are considered in the preselection as well, where fe corresponds to a forward electron [19]. Thus, the Z boson selection applied as tag criteria are intended to single out $Z \to e^+e^-$ processes and further tighten the cuts applied in the preselection. These cuts are largely based on [19].

- The ATLAS data set has several background flags for events, which are checked true if the event meets certain background criteria. One important source of background for this analysis is beam-induced-background (BIB): High-energy muons can penetrate the shielding designed to mitigate BIB, and deposit high energies in the calorimeters, which may lead to a false jet reconstruction [20]. Thus, BIB rejection tools are used to identify these fake jets [20]. Making use of these tools, the first cut of this event selection accesses the output as event flags, and rejects event with a relevant flag set to true.

- As covered before, a bias in efficiencies occurs when the jets used to calculate the efficiency has triggered the event itself. This tag Z selection is used to circumvent this bias, but as a precaution it is useful to explicitly check which trigger has triggered the event. Thus, only events that were triggered by a selected electron trigger with a threshold appropriate for electrons in a Z decay are kept. In this case, the "HLT_e26_lhtight_ivarloose_L1eEM26M" trigger was chosen as a Phase-I low threshold electron trigger.

- For the next cut in the event selection, a number of different criteria for the electrons in the event are applied:

  - First, there must be a primary vertex in the event associated with the electron.

  - Next, the Pseudorapidity of the central calorimeter cluster must be in a range of $|\eta| < 2.47$, which corresponds mostly to the electron Pseudorapidity. This rejects electrons outside of the reconstruction limit of electrons, which is limited by the ID coverage [21].
  - Then, the d_0 significance is used, which is defined as the ratio of the impact parameter to total its error [22], and can be used to select particles with correctly reconstructed tracks from the primary vertex. Accordingly, only tracks with $|d_0$ significance$| < 5$ are selected.
  - Furthermore, the electron isolation is investigated. The isolation is quantified using the sum of topo-cluster E_T in a cone of $dR = 0.2$ around the electron, called *topoetcone20* [12]. The electrons are then cut at topoetcone20 $< \max(0.015 \cdot p_T, 3.5\text{GeV})$.
  - And finally, the electrons must have a transverse momentum greater than $p_T = 20$ GeV.

  Events containing less than two electrons passing these criteria are rejected.

- The mass of the Z boson is very well-known at $m_Z = (91.1876 \pm 0.0021)$ GeV [23], which allows for a further restrictions on the events. Accordingly, the two leading electrons in transverse momentum must have a combined invariant mass between $m_{\text{lower}} = 76.2$ GeV and $m_{\text{upper}} = 106.2$ GeV.

- For the final cut, the neutral charge of the Z boson is used: In $Z \to e^+e^-$ events, the two leptons must always have opposite charge. Thus, all events where the two reconstructed electrons do not have opposite charge are discarded.

5.6 Legacy and Phase-I Jet Efficiencies

Before the object-level jet efficiency can be calculated, TOB and offline jet geometry matching needs to be performed. This eliminates cases where the amount of identified TOBs above the threshold correctly matches the amount of offline jets above the threshold, but where one TOBs energy was in reality overestimated to pass the threshold, while another TOBs energy was underestimated. Geometry matching would identify that the wrong TOB was triggered and count the corresponding jet as inefficient.
The geometry matching is implemented as follows: For each offline jet in the event, the jet TOB closest in ΔR is selected. If ΔR between the offline jet and its closest TOB is smaller than $\Delta R < 0.4$, the offline jet and the TOB are considered matched.
Using matched offline jet and TOB pairs, the efficiency calculation can be performed. The behaviour of the trigger is emulated by applying an energy threshold to the TOB that was just matched to an offline jet. If the TOB lies below the threshold, it is counted as an inefficiency, and if it lies above the threshold, as efficient. Thus, the efficiency is defined as

$$\varepsilon = \frac{\text{Number matched TOBs with } E > E_{th}}{\text{Number of offline jets}}. \tag{2}$$

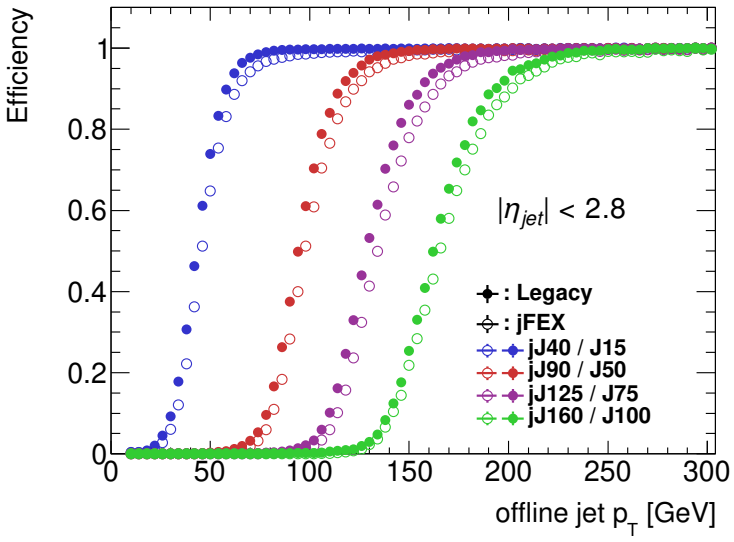

Figure 20: Jet trigger efficiency for four different Legacy and jFEX triggers. The trigger name contains the trigger level (L1), optionally the jFEX identifier (j), as well as the trigger criterion. jFEX thresholds are calibrated towards the offline jet energy, corresponding to a single jet TOB above 28/68/124/161.

This efficiency is commonly calculated as a function of offline jet p_T, which shows the characteristic trigger resolution as described previously. By setting a different energy threshold E_{th}, the efficiencies for any jet trigger can be calculated. The efficiency calculation can be done analogously for the Legacy trigger and both the jFEX and gFEX components of the Phase-I trigger systems by choosing the corresponding Legacy, jFEX or gFEX TOBs for the matching procedure. The jet trigger efficiencies for four different single jet triggers for Legacy and jFEX can be found in Figure 20, gFEX is shown separately in Figure 21. The efficiency plots clearly show the characteristic turn-on curves. For triggers with a higher threshold energy, the turn-on is shifted to the right as expected. The Legacy system reaches the plateau nicely, just as the Phase-I system jFEX triggers, and both systems align well. The gFEX triggers show inefficiencies in these object-level single-jet efficiencies.
While differences in efficiency between Legacy and Phase-I can be observed, these efficiencies can not be used for a fair comparison in performance of the two systems, since the rate of the respective trigger plays a crucial role for performance. Thus, efficiency-matched rates will be discussed in Section 7.

5.7 Geometric Jet Efficiencies

While jet efficiencies are mostly plotted as a function of offline jet p_T to reveal the characteristic energy resolution, other observable may be interesting to find the origin of inefficiencies in the detector, such as the geometric coordinates η and ϕ. To visualise dips in the efficiency, a p_T cut on offline jets is applied to only consider jets close to the plateau of the p_T efficiency.
The jet trigger efficiencies as a function of Pseudorapidity η can be found in Figures 22, 23 and

24 for Legacy, jFEX and gFEX respectively. Note that the absolute efficiency values in these plots may not be used for a comparison between the systems, as the manually placed p_T cut is set to different values, which is necessary due to the jFEX trigger threshold calibration. Only the relative size of the dips to each other can be used for further discussion.
For both Legacy and Phase-I, dips at approximately $|\eta| = 1.7$, $|\eta| = 2.5$ and $|\eta| = 3.2$ can be observed, which can be explained by the calorimeter structure:

- The inner dip at $|\eta| = 1.7$ is approximately located at the so-called crack region, where a large amount of material is located in front of the calorimeters. A corresponding plot can be found in the appendix A.3, where the crack region is visualised.
- The dip at $|\eta| = 2.5$ could be caused by several effects: First, at $|\eta| = 2.5$ the granularity of input trigger towers becomes coarser for both legacy and jFEX [6]. Secondly, the granularity of cells in both the EMEC and HEC is decreased as well [6]. The change in granularity could cause a bias in the TOB position, which would then cause a dip in the efficiency.
- The outer dip at $|\eta| = 3.2$ is located at the end of the high granularity LAr Barrel and Endcap, and at the start of the FCal, where the cell granularity becomes coarser [6]. The relative dip in efficiency is more prevalent for the legacy system since the legacy jet trigger coverage ends at $|\eta| = 3.2$, while the Phase-I system coverage extends into the forward regions as mentioned in Section 3.

The efficiencies can be visualised in the $\eta \times \phi$ plane as well, as seen in Figures 25a to 25c. As the ATLAS detector is mostly symmetrical in ϕ, the ϕ coordinate has a negligible influence on the efficiency. The same dips in η that could be located in the previous plots are visible here as well. Note that no p_T cut is applied for the efficiency maps.

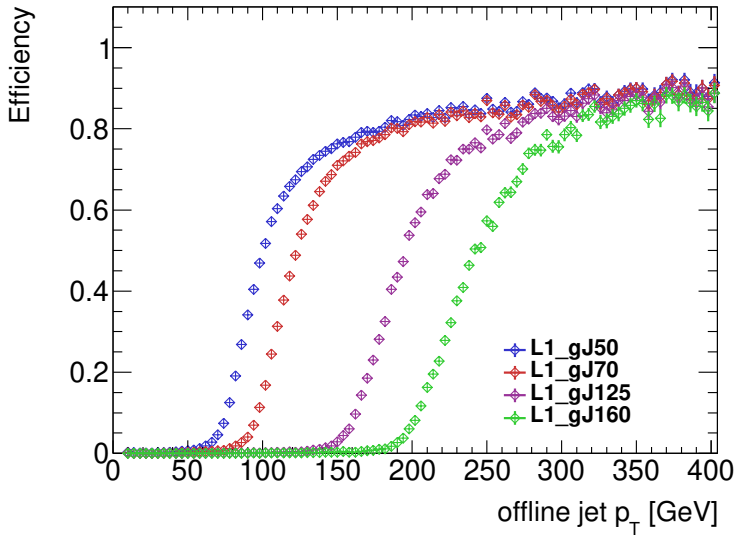

Figure 21: Jet trigger efficiency for four different gFEX triggers. The trigger name contains the trigger level (L1), the gFEX identifier (g), as well as the trigger criterion (A single jet with TOB energy above x → gJx).

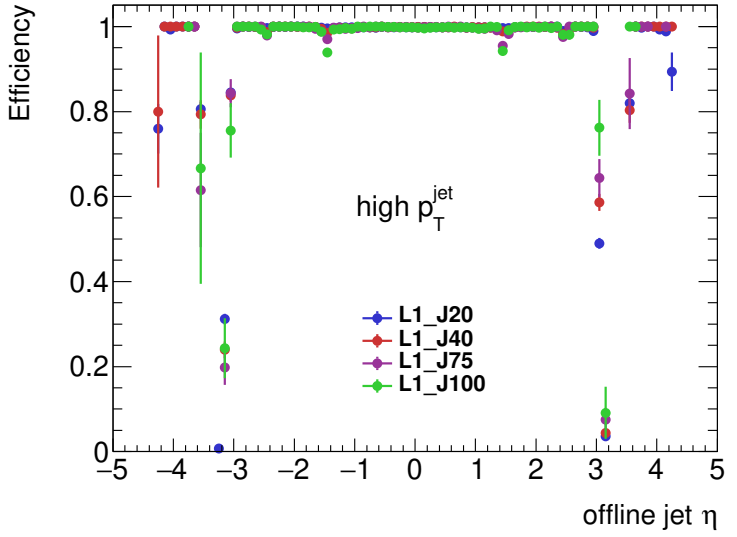

Figure 22: Jet trigger efficiency as a function of Pseudorapidity for four different Legacy triggers. A p_T cut is applied to only consider the plateau. The trigger name contains the trigger level (L1), as well as the trigger criterion (A single jet with TOB energy above x → Jx).

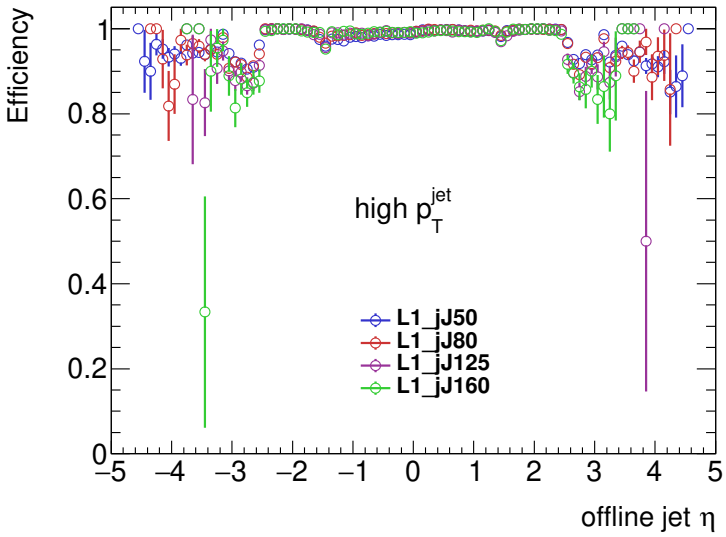

Figure 23: Jet trigger efficiency as a function of Pseudorapidity for four different jFEX triggers. A p_T cut is applied to only consider the plateau. The trigger name contains the trigger level (L1), the jFEX identifier (j), as well as the trigger criterion calibrated towards the offline jet energy, corresponding to a single jet TOB above 44/68/124/161.

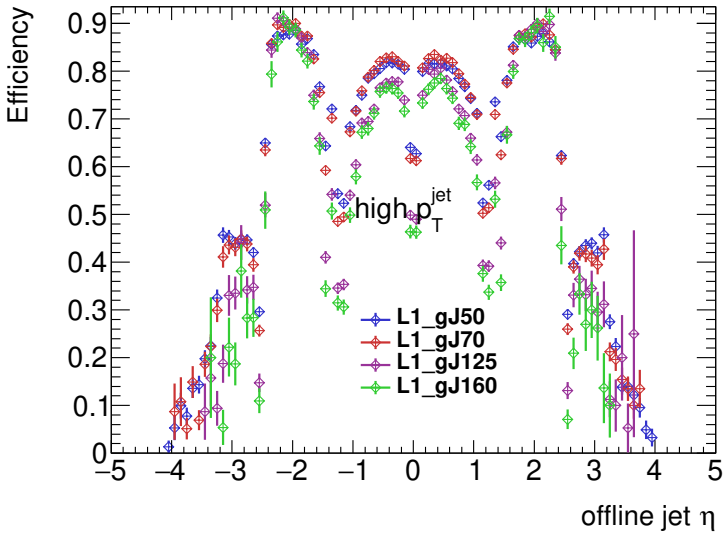

Figure 24: Jet trigger efficiency as a function of Pseudorapidity for four different gFEX triggers. A p_T cut is applied to only consider the plateau. The trigger name contains the trigger level (L1), the gFEX identifier (g), as well as the trigger criterion (A single jet with TOB energy above x → gJx).

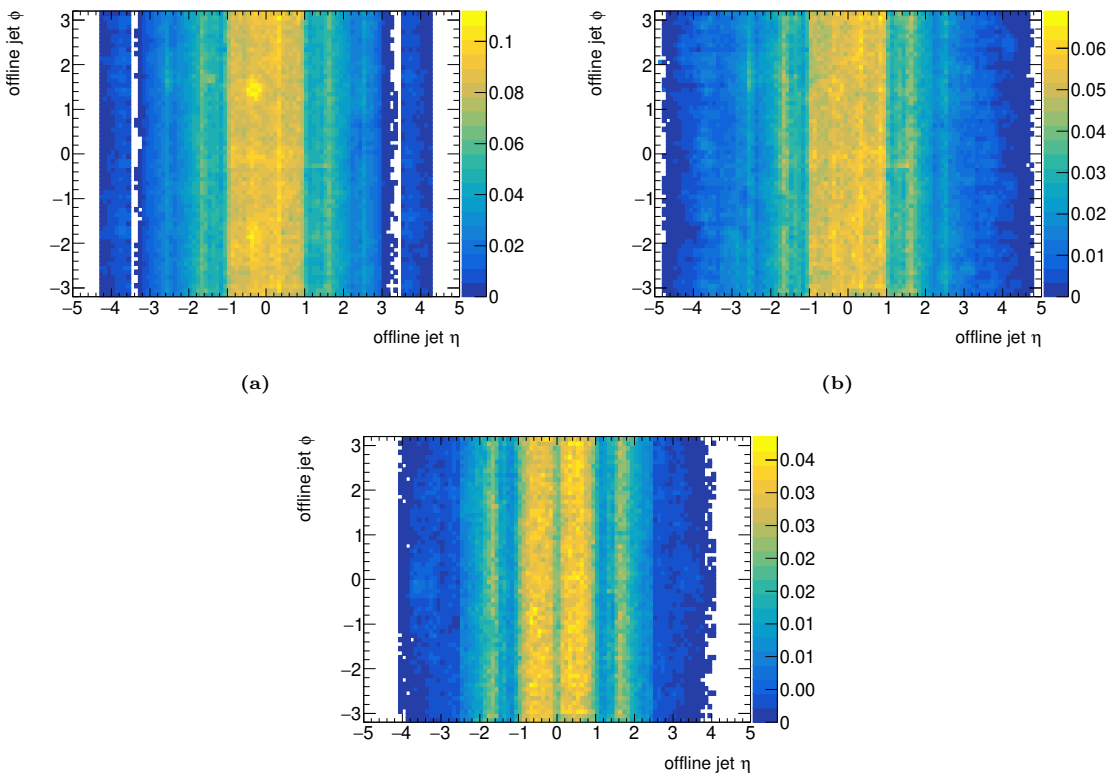

(a) **(b)**

(c)

Figure 25: Jet trigger efficiency in η and ϕ for the L1_J20 (a), L1_jJ50 (b) and L1_gJ50 (c) triggers.

6 Level-1 Multi-jet Trigger Efficiencies

The second goal of this analysis is to determine the L1 trigger efficiency for many different multi-jet triggers. This calculation was integrated into the environment of the single-jet efficiencies. Thus, the exact same framework, data and event selection are used. The crucial distinctions are made in the efficiency calculation itself.

- First, as opposed to the single-jet trigger efficiencies calculated in the previous sections, the multi-jet efficiencies are event level efficiencies: An event is only triggered if n jet TOBs above the respective trigger threshold E_{th} were identified. Here, n corresponds to the multiplicity of the trigger.
- In principal, performing TOB and offline jet matching is not necessary when determining event level efficiencies, since the event being triggered is the focus rather than correct identification of the TOB. However, matching is still performed for multi-jets, as it circumvents an efficiency bias at low energies: Since electrons can produce jet TOBs as well from energy depositions in the calorimeters, these fake jet TOBs can contribute significantly to the overall efficiency at low energies. TOB and offline jet matching eliminates these fake TOBs in the efficiency calculation due to the geometric matching in η and ϕ.
- Another distinction is made inside the TOB and offline jet matching process: When investigating multi-jet events, cases exist where multiple jets are found in close proximity to each other, for example two jets occurring in opposite direction of the Z boson. Accordingly, it is important to check whether multiple offline jets were matched to the same TOB. This duplicate checking was implemented as an addition to the standard TOB and offline jet matching process.

Finally, the efficiency for multi-jet events is defined as seen in Equation 3.

$$\varepsilon = \frac{\text{Number of events with } n \text{ matched TOBs with } E > E_{th}}{\text{Number of events with at least } n \text{ offline jets}} \tag{3}$$

Multi-jet efficiencies are commonly displayed as a function of the n-th leading jet p_T. Figure 26 shows the three-jet efficiency for Legacy and jFEX for several different thresholds, while four-jet efficiencies are shown in Figure 27. Due to the inefficiencies on object-level for gFEX, gFEX multi-jet efficiencies were not pursued any further.
In both plots Legacy and jFEX line up well within the margins of error. Since multiple jets occur much less frequently in Z boson events than single events, the relative errors are significantly higher than before.

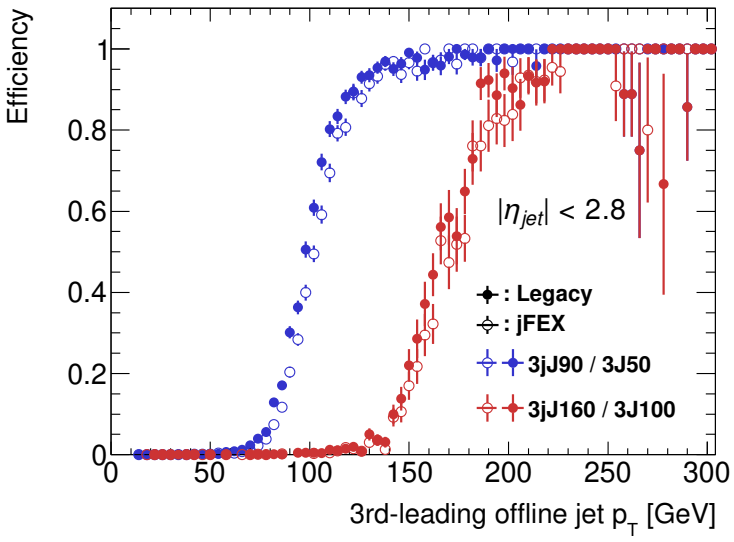

Figure 26: 3-Jet trigger efficiency for two different Legacy and jFEX triggers. The jFEX trigger thresholds are calibrated towards the offline jet energy, corresponding to TOB thresholds of 83 and 161.

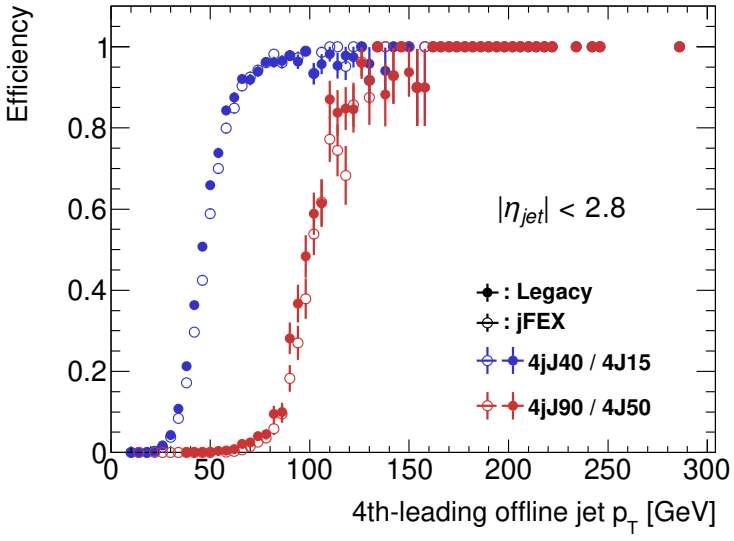

Figure 27: 4-Jet trigger efficiency for two different Legacy and jFEX triggers. The jFEX trigger thresholds are calibrated towards the offline jet energy, corresponding to TOB thresholds of 28 and 83.

7 Efficiency-matched Trigger Rates

Even though the efficiencies for both Legacy and Phase-I were calculated successfully, the results do not allow for a direct comparison in performance between the two systems. To evaluate the performance of a trigger system, the trigger rate needs to be taken into account.
A high efficiency is inherently good for the performance of a trigger. However, a hypothetical trigger that triggers every single event and does not reject any events would have perfect efficiency of $\varepsilon = 1$ for all energies, yet it would not perform well as a trigger, as its purpose to trigger relevant events while rejecting background is unfulfilled. Thus, it is crucial to look at the trigger rate as well when evaluating performance. A performing trigger is a trigger with a good efficiency, while maintaining a relatively low rate, taking up less space in the ATLAS L1 trigger rate budget. To evaluate the performance of the Legacy and Phase-I systems, efficiency-matched trigger rates are implemented in this analysis to achieve a direct comparison method between the two systems.
The idea of efficiency-matched trigger rates is to find a fair comparison point between two triggers. This is achieved by matching the efficiency curves to find a set of triggers with similar efficiencies at a certain offline jet energy point. Integrated rates are then calculated and compared for these triggers.
As the used data should be triggered proportional to the instantaneous Luminosity, a so-called Zero Bias trigger is used, which fires one LHC revolution after a high-p_T electron trigger. The electron trigger is less susceptible to pile-up interactions, making it as proportional as possible to the Luminosity [24].

7.1 Integrated Rate Calculation

The rate comparison is done by calculating the integrated rate of a trigger over one run. For this analysis, run 456729 was selected as one of the larger runs of Run-3.
First, the Zero Bias data is analysed, recording the amount of events that were triggered. In the case of single-jet efficiencies, all events with at least one TOB above the threshold are counted. On the contrary, for multi-jet efficiencies multiple TOBs need to surpass the energy threshold. Additionally, a Pseudorapidity cut is applied to the TOBs to be able to compare Legacy and Phase-I at $|\eta| < 3.1$. The number of events N_{ev} is calculated for each Luminosity block, which are the sections of approximately equal Luminosity in a run.
Next, the run information is retrieved, containing the duration of each Luminosity block, as well as the rate of the zero bias trigger. By summing over all Luminosity blocks, the run duration t_{run}, as well as the average zero bias rate $f_{\text{av.}}^{\text{ZeroBias}}$ are determined.
Additionally, the number of colliding bunches $b_{\text{colliding}} = 2452$ for run 456729 and the number of total bunches $b_{\text{total}} = 3564$ are used in the calculation.
The integrated rate f_{int} is then defined as

$$f_{\text{int}} = \frac{N_{ev}}{t_{\text{run}}} \cdot \frac{40\,\text{MHz}}{f_{\text{av.}}^{\text{ZeroBias}}} \cdot \frac{b_{\text{colliding}}}{b_{\text{total}}}. \tag{4}$$

The 40 MHz correspond to the approximate LHC bunch crossing rate. The error is determined through simple propagation of uncertainty of N_{ev} and $f_{\text{av.}}^{\text{ZeroBias}}$.

7.2 Performance Evaluation

Efficiency matching is performed by manually checking the efficiency turn-ons for different triggers. A good match at the $\varepsilon = 0.5$ point has been found for the L1_J50, L1_jJ90 and L1_gJ50 and L1_J100, L1_jJ160, L1_gJ100 triggers for single-jet efficiencies, as well as the L1_nJ50 and L1_njJ90 for multi-jet efficiencies. As stated in the previous section, gFEX multi-jet efficiencies were not investigated in this thesis. The corresponding efficiency curves are found in Figures 28a to 29b for single-jet, 3-jet and 4-jet triggers. Using the integrated rate formula shown in Equation 4, the rates for all trigger sets are shown in Table 3.

For single-jet efficiencies, gFEX and Legacy show similar rates within the margins or error, while jFEX shows rate improvements compared to the Legacy system. For multi-jet efficiencies, the relative errors are too high to compare the rates effectively, since the amount of multi-jet events in a single run is too low, yet the rates seem to be similar for Legacy and jFEX.

There are several factors that could contribute to the rate improvement in jFEX compared to Legacy: The finer input granularity results in better pile-up rejection, causing less pile-up events to be triggered. Additionally, the jFEX jet algorithm is working with round $R < 0.4$ jets, while the Legacy algorithm uses rectangular 4×4 jet elements.

Taking both rate and efficiency into account, jFEX performs well in both single-jet and multi-jet events, showing a similar efficiency and an improved rate compared to the Legacy system. gFEX shows significant inefficiencies in object-level single-jet efficiencies, while maintaining a similar rate to the Legacy system. Since the main purpose of gFEX is to measure global observables such as E_T^{miss} and large-R jets, which it is designed for using only a single board for the entire detector range, this result is ultimately not considered troubling.

Nevertheless, the Phase-I system is well equipped for Run-3, with jFEX showing a promising jet trigger performance.

Trigger	Integrated Rate f_{int} [kHz]
L1_J50	38.2 ± 1.5
L1_jJ90	31.8 ± 1.4
L1_gJ50	37.6 ± 1.5
L1_J100	2.9 ± 0.4
L1_jJ160	2.5 ± 0.4
L1_gJ100	2.9 ± 0.4
L1_3J50	0.63 ± 0.20
L1_3jJ90	0.69 ± 0.21
L1_4J50	0.06 ± 0.06
L1_4jJ90	0.13 ± 0.09

Table 3: Integrated trigger rates for three different sets of Legacy, jFEX and gFEX triggers in run 456729. An $|\eta| < 3.1$ cut was applied on the TOBs for all rate calculations.

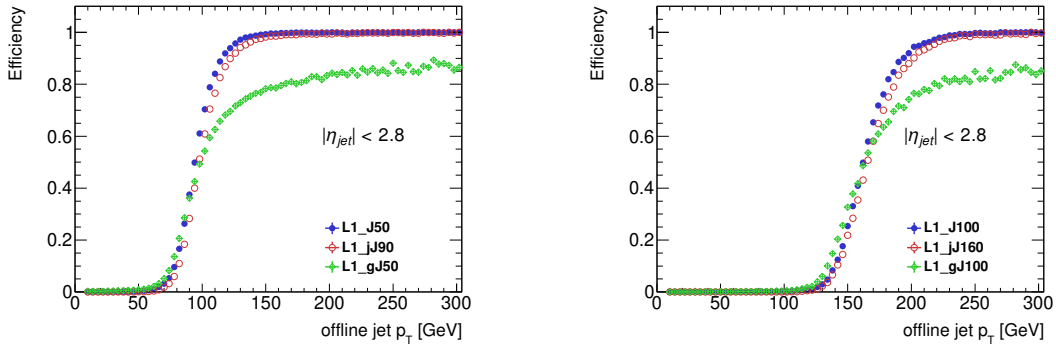

(a) (b)

Figure 28: Comparison of Legacy, jFEX and gFEX single-jet triggers with similar turn-ons for (a) the L1_J50, L1_jJ90 and L1_gJ50 and (b) the L1_J100, L1_jJ160 and L1_gJ100.

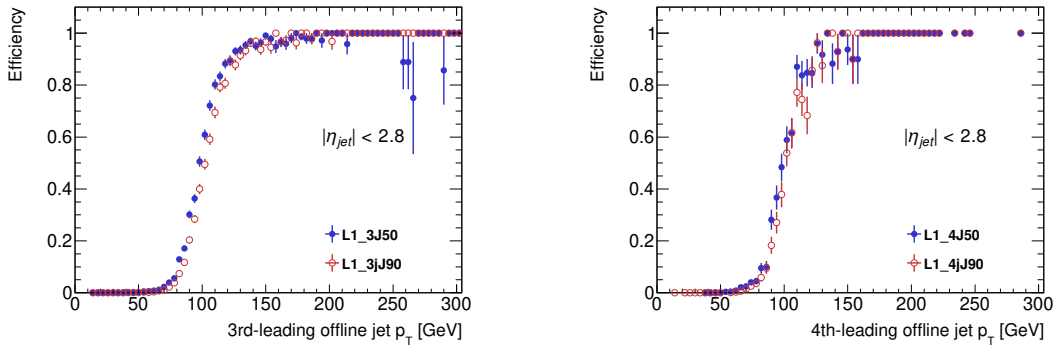

(a) (b)

Figure 29: Comparison of Legacy and jFEX multi-jet triggers with similar turn-ons for (a) the L1_3J50, and L1_3jJ90 and (b) the L1_4J50, and L1_4jJ90.

8 Summary and Conclusion

To challenge the increased average pile-up in Run-3, the ATLAS detector has updated its Level-1 trigger system during the Phase-I upgrade from 2019 to 2022. The two new feature extractors responsible for jet identification introduced in the Phase-I trigger system, jFEX and gFEX, are studied for their jet trigger performance compared to the Legacy system in this thesis using Run-3 data during the commissioning phase at $\sqrt{s} = 13.6$ TeV.

A jet efficiency framework is implemented, including jet cleaning, jet and electron calibration, as well as overlap removal, enabling an accurate efficiency calculation. Object-level single-jet efficiencies are determined using a Z event selection, making use of the tag-and-probe method. Using the same selection, multi-jet efficiencies are calculated on event-level. Finally, integrated trigger rates are calculated and compared for different Legacy and Phase-I triggers with matching efficiencies for performance evaluation.

Legacy and jFEX are showing similar single-jet and multi-jet efficiencies, while gFEX shows significant inefficiencies on object-level, and was thus only considered for the single-jet performance comparison. When comparing single-jet trigger rate for the L1_J50 and L1_J100 and their respective jFEX and gFEX equivalents, gFEX and Legacy rates match within the margins of error, while jFEX rates are lower, which can be largely attributed to the different jet identification algorithm and improved pile-up rejection due to higher input granularity. For 3-Jet and 4-Jet trigger rates, Legacy and jFEX match within the margins or error, although the relative error is too large to resolve small differences.

In conclusion, jFEX shows a promising performance, while gFEX performs significantly worse for jets on object-level. This result is in essence not considered concerning, due to gFEX design prioritising global observables and large-R jets.

This analysis shows that Phase-I is well equipped for Run-3. jFEX and the Phase-I system introduce promising changes, such as the ability to calibrate jets on object level to counteract inefficiencies in specific eta regions or the digitised input data, while not only maintaining a similar rate and efficiency to the Legacy system, but improving the trigger rate. Yet, improvements can still be made by tuning the jFEX noise cuts in the future, as jFEX noise cuts are currently set to constant values as demonstrated. Using resimulated TOBs with different noise cuts, the effect of noise cuts on efficiency and rate can be studied, which is currently being investigated for 2024 data taking.

A Appendix

A.1 Luminosity

The Luminosity $\mathcal{L}$, also referred to as instantaneous Luminosity, is a value from scattering theory that describes the ratio of number of events detected per second to the differential cross section σ. It is defined as

$$\mathcal{L} = \frac{dN}{\sigma dt},$$

and it is a useful variable to assess the performance of particle accelerators. At the LHC, the instantaneous Luminosity can be expressed as a function of beam parameters such as the number of protons in each bunch N_i, the number of bunches n_b, the revolution frequency f_{rev} and the horizontal - and vertical - beam spreads σ_x and σ_y respectively:

$$\mathcal{L} = \frac{N_1 N_2 f_{\text{rev}} n_b}{4\pi\sigma_x\sigma_y}$$

The integrated Luminosity then is defined as

$$\mathcal{L}_{\text{int}} = \int \mathcal{L}\, dt,$$

and describes the size of the collected data set.

A.2 Pseudorapidity

The Pseudorapidity η is a variable used to describe the cylindrical detector geometry of the ATLAS detector. It is related to the polar angle θ by

$$\eta = -\ln\left(\tan\left(\theta/2\right)\right).$$

Together with the azimuthal angle ϕ, it describes the coordinate system of the ATLAS detector.

A.3 Crack Region

In the so-called crack region, a large amount of material is located in front of the calorimeters [25]. Figure 30 shows the cumulative amounts of material in units of radiation length X_0 as a function of η. The crack region can be clearly identified at $\eta \approx 1.7$.

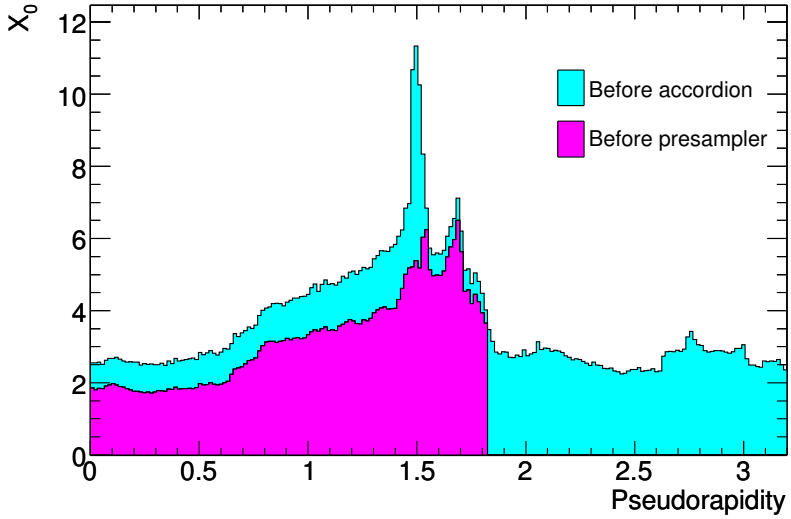

Figure 30: Cumulative amounts of material, in units of radiation length X_0 and as a function of abs eta, in front of and in the electromagnetic calorimeters. The plot shows separately the total amount of material in front of the presampler layer and in front of the accordion itself over the full eta-coverage [25].

References

[1] ATLAS Collaboration. Observation of a new particle in the search for the standard model higgs boson with the ATLAS detector at the LHC. *Physics Letters B*, 716(1):1–29, sep 2012. URL https://doi.org/10.1016%2Fj.physletb.2012.08.020.

[2] CMS Collaboration. Observation of a new boson at a mass of 125 GeV with the CMS experiment at the LHC. *Physics Letters B*, 716(1):30–61, sep 2012. URL https://doi.org/10.1016%2Fj.physletb.2012.08.021.

[3] ATLAS Collaboration. Search for non-resonant pair production of Higgs bosons in the $b\bar{b}b\bar{b}$ final state in pp collisions at $\sqrt{s} = 13$ TeV with the ATLAS detector. Technical report, CERN, Geneva, 2022. URL https://cds.cern.ch/record/2811390.

[4] M. Schott. *Study of the Z Boson Production at the ATLAS Experiment with First Data*. PhD thesis, Ludwig-Maximilians-Universität München, 2007.

[5] L. R. Evans and P. Bryant. LHC Machine. *JINST*, 3:S08001, 2008. URL http://cds.cern.ch/record/1129806.

[6] ATLAS Collaboration. The ATLAS Experiment at the CERN Large Hadron Collider: A Description of the Detector Configuration for Run 3. Technical report, CERN, Geneva, 2023. URL https://cds.cern.ch/record/2859916.

[7] ATLAS Collaboration. Performance of pile-up mitigation techniques for jets in pp collisions at $\sqrt{s} = 8$ TeV using the ATLAS detector. Performance of pile-up mitigation techniques for jets in pp collisions at $\sqrt{s} = 8$ TeV using the ATLAS detector. *Eur. Phys. J. C*, 76:581, 2016. URL https://cds.cern.ch/record/2058295.

[8] ATLAS Collaboration. The ATLAS Level-1 Calorimeter Trigger. Technical report, CERN, Geneva, 2008. URL http://cds.cern.ch/record/1080560.

[9] L1Calo Internal Communication. Documentation of the L1Calo algorithm specifications, 8.2.2023. URL https://gitlab.cern.ch/l1calo-run3-simulation/documentation/Run3L1CaloOfflineSWReqs/-/blob/master/l1caloreqs.pdf?ref_type=heads.

[10] M. Hesping Internal Communication. jFEX: Status & Expected Performance, TDAQ week, 14.3.2024. URL https://indico.cern.ch/event/1382847/contributions/5813532/attachments/2819621/4923424/2024-03-14-jfex-status-tdaq-week.pdf.

[11] ATLAS Collaboration. Performance of the upgraded PreProcessor of the ATLAS Level-1 Calorimeter Trigger. *JINST*, 15(11):P11016, 2020. URL https://cds.cern.ch/record/2717655.

[12] ATLAS Collaboration. Electron and photon performance measurements with the ATLAS detector using the 2015-2017 LHC proton-proton collision data. *JINST*, 14(12):P12006, 2019. URL https://cds.cern.ch/record/2684552.

[13] ATLAS Collaboration. Jet reconstruction and performance using particle flow with the ATLAS Detector. Jet reconstruction and performance using particle flow with the ATLAS Detector. *Eur. Phys. J. C*, 77(7):466, 2017. URL https://cds.cern.ch/record/2257597.

[14] ATLAS Collaboration. Selection of jets produced in 13TeV proton-proton collisions with the ATLAS detector. Technical report, CERN, Geneva, 2015. URL https://cds.cern.ch/record/2037702.

[15] ATLAS Collaboration. The ATLAS Collaboration Software and Firmware. Technical report, CERN, Geneva, 2021. URL https://cds.cern.ch/record/2767187.

[16] ATLAS Collaboration. Electron and photon energy calibration with the ATLAS detector using 2015-2016 LHC proton-proton collision data. *JINST*, 14(03):P03017, 2019. URL https://cds.cern.ch/record/2650720.

[17] ATLAS Collaboration. Jet energy scale and resolution measured in proton–proton collisions at $\sqrt{s} = 13$ TeV with the ATLAS detector. *Eur. Phys. J. C*, 81(8):689, 2021. URL https://cds.cern.ch/record/2722869.

[18] ATLAS Collaboration. Recommendations of the physics objects and analysis harmonisation study groups 2014. ATLAS Note: 4.2.2015. URL https://cds.cern.ch/record/1700874/files/ATL-COM-PHYS-2014-451.pdf.

[19] D. Raßloff. *Installation, Commissioning and Calibration of the ATLAS Level-1 Calorimeter Trigger in Run 3*. PhD thesis, Ruprecht-Karls-Universität Heidelberg, 2023.

[20] R. Bruce et al. Characterisation and mitigation of beam-induced backgrounds observed in the ATLAS detector during the 2011 proton-proton run. Technical report, CERN, Geneva, 2012. URL https://cds.cern.ch/record/1449809.

[21] ATLAS Collaboration. Electron reconstruction and identification in the ATLAS experiment using the 2015 and 2016 LHC proton-proton collision data at $\sqrt{s} = 13$ TeV. *Eur. Phys. J. C*, 79(8):639, 2019. URL https://cds.cern.ch/record/2657964.

[22] ATLAS Collaboration. *ATLAS inner detector: Technical Design Report, 1*. Technical design report. ATLAS. CERN, Geneva, 1997. URL https://cds.cern.ch/record/331063.

[23] R.L. Workman et al. (Particle Data Group). Prog.theor.exp.phys. 2022, 083c01 (2022) and 2023 update. URL https://pdg.lbl.gov/2023/tables/rpp2023-sum-gauge-higgs-bosons.pdf.

[24] ATLAS Collaboration. Operation of the ATLAS trigger system in Run 2. *JINST*, 15(10):P10004, 2020. URL https://cds.cern.ch/record/2725146.

[25] ATLAS Collaboration. The ATLAS Experiment at the CERN Large Hadron Collider. *JINST*, 3:S08003, 2008. URL https://cds.cern.ch/record/1129811.

Acknowledgements

First and foremost, I would like to thank Prof. Dr. Hans-Christian Schultz-Coulon for providing me with the opportunity for this bachelors thesis, as well as Prof. Dr. Stephanie Hansmann-Menzemer for agreeing to be second referee. Additionally, I would like to thank Sebastian Weber, Damir Raßloff, and Martin Wessels for their guidance and supervision throughout the completion of this thesis, as well as the entire KIP F8/F11 group for all the great experiences.
Special thanks to Anna, David, Furkan, Jan, Laura, Marius, Mathias, Moritz, Thomas, Tobias, and Rainer, who all contributed valuable feedback to this thesis.
Lastly I am grateful for Dr. med. Christoph Deinzer, Dr. med. Katrin Benzler, Dr. med. Mary Carter, everyone at Station 85 of the Medizinische Uniklinik Tübingen, and most importantly my family, for their support during my chemotherapy, which briefly interrupted the work for this thesis.

Erklärung

Ich versichere, dass ich diese Arbeit selbstständig verfasst und keine anderen als die angegebenen Quellen und Hilfsmittel benutzt habe.
Heidelberg, den 29.5.2024,

Felix Fl